

Article

Boxy/Peanut Bulges: Comparative Analysis of EGIPS Galaxies and TNG50 Models

Anton Smirnov ^{1,*}, Alexander Marchuk ^{1,2}, Viktor Zozulia ^{1,2}, Natalia Sotnikova ^{1,2} and Sergey Savchenko ^{1,2}

¹ Central (Pulkovo) Astronomical Observatory of the Russian Academy of Sciences, Pulkovskoye Chaussee 65/1, 196140 St. Petersburg, Russia; a.a.marchuk+astro@gmail.com (A.M.); vdzozulia.astro@gmail.com (V.Z.); n.sotnikova@spbu.ru (N.S.); s.s.savchenko@spbu.ru (S.S.)

² St. Petersburg State University, Universitetskij pr. 28, 198504 St. Petersburg, Russia

* Correspondence: zeleniikot@gmail.com

Abstract

We investigated the properties of boxy/peanut-shaped (B/PS) bulges in a sample of 71 galaxies from the Edge-on Galaxies in the Pan-STARRS Survey (EGIPS) and 20 simulated galaxies from Illustris TNG50 using multicomponent photometric decomposition. For each real and simulated galaxy, we obtained a suitable photometric model in which the B/PS bulge was represented by a dedicated 2D photometric function. For real galaxies, we found that more flattened X-structures are generally residing in larger B/PS bulges. When tested against the galaxy masses, we verified that both larger bulges and more flattened X-structures are typically found in more massive galaxies. Since large bars are also known to reside in more massive galaxies, we conclude that the flatness of X-structures in larger B/PS bulges has a physical origin, rather than being solely a result of projection effects due to differences in observed bar viewing angles. When comparing the properties of B/PS bulges between EGIPS galaxies and TNG50 galaxies, with bars rotated for different viewing angles, we found that B/PS bulges in TNG50 are considerably smaller and less luminous in terms of total intensity. This is consistent with previous studies of bar properties in TNG50, indicating the B/PS bulges in TNG50 differ from those in real galaxies, as do their parent bars.

Keywords: galaxies: bulges; galaxies: photometry; galaxies: structure; galaxies: bar

1. Introduction

Boxy and peanut-shaped (B/PS) bulges are a distinct type of stellar subsystem frequently observed in the central regions of edge-on disc galaxies, distinguished by their morphology and dynamical properties [1–7]. These bulges are believed to be intrinsically linked to the bars, being the extension of the latter in the direction perpendicular to the disc plane. This implies that the “building blocks” of galaxies, namely the 3D regular stellar orbits of stars, constituting bars viewed face-on and boxy/peanuts viewed edge-on are essentially the same [8,9]. The fact that the growing bars are usually not confined to the disk plane has been proved in numerous simulation studies [10–21]. Conversely, it is commonly assumed that every observed boxy/peanut-shaped bulge originates from a corresponding bar. Direct evidence supporting this has been obtained for a sample of galaxies with B/PS bulges through kinematical analyses, which show that these structures exhibit cylindrical rotation [22,23]. Furthermore, when a stellar disk is viewed at slight or moderate inclination, both the boxy/peanut features and the planar bar can be simultaneously observed [4,24,25].



Received: 2 December 2025

Revised: 26 December 2025

Accepted: 29 December 2025

Published:

Copyright: © 2025 by the authors.

Licensee MDPI, Basel, Switzerland.

This article is an open access article distributed under the terms and conditions of the [Creative Commons Attribution \(CC BY\) license](#).

This study primarily focuses on the observational properties of boxy/peanuts. Consequently, the theoretical developments in the field, including orbital studies and studies of B/PS bulges formation mechanisms, are not discussed in extensive detail. Instead, we limit ourselves to highlighting a few key facts that are also significant from an observational standpoint.

First, the bulge morphology, whether boxy or peanut-shaped, is largely determined by the so-called bar viewing angle, an angle between the line of sight (LoS) and the bar major axis. In general, the closer the bar major axis is aligned with the LoS (end-on view), the more boxy the bulge appears, whereas the most pronounced peanut morphology is observed when the bar major axis is oriented perpendicular to the LoS (side-on view).

A second note concerns terminology. Above the disk plane the, B/PS bulges frequently exhibit distinctive intensity enhancements that have an X-like shape. Those are usually referred as “X-structures” and sometimes understood as a separate entity from underlying B/PS bulge. However, the orbital studies tell us that no orbits constitute the B/PS bulge and X-structures separately, but the latter make their appearance due to nature of orbits in the B/PS bulge [26–28]. The stars moving along 3D orbits in B/PS bulge prefer to stay longer times at some specific points, typically furthest from the center and highest from the disk plane. The X-structure rays are formed by alignment of such points for orbits with different extensions of major axes in physical space.

From an observational perspective, B/PS bulges are rather complicated objects to study. This complexity primarily stems from the fact that they are observed in the central regions of edge-on or nearly edge-on galaxies, where the line-of-sight (LoS) intensity represents the superposition of multiple structural components, e.g., the B/PS itself and the stellar disk. Additional structural features, including other types of bulges and rings, may also be present. It is well-known that, except B/PS bulges, central parts of galaxies can host two other types of bulges [29–31]: classical ones, usually viewed as the remnants of minor galaxy merges, and the so-called pseudobulges, forming through the bar-induced gas inflow to the galaxy central regions. Because different bulge types can coexist within the same galaxy, interpreting observational results can be challenging, as one may entirely miss to which physical component observable properties such as bulge-to-total ratio (B/T), scale lengths, etc., should be attributed. Nevertheless, boxy/peanuts are important objects to study since they provide a unique possibility to study bars vertical structure, the properties of which should be somehow connected with conditions in the stellar disk, where the bar is formed.

Observational studies of B/PS bulges are vast in scope, ranging from statistical studies [1–6], which provide important information on the abundance of B/PS bulges in the local Universe and beyond [24], to more sophisticated analyses, including the isophotal analysis [4,32], structural analysis via unsharp-masking [33], and photometric decomposition [34,35]. So far, it has been found that B/PS are observed in nearly 20–40% of disk galaxies, and the frequency strongly depends on the host galaxy mass, showing a sharp increase at $M \gtrsim 10^{10.3-10.4} M_{\odot}$ [6,7].

As for the structural parameters, B/PS bulges typically exhibit a substantial contribution to the total galaxy luminosity, quantified by the bulge-to-total ratio B/T , with median values for different samples ranging from about 0.2 to 0.5 [7] (keep in mind that the B/T values referred to here are obtained by means of automatic bulge plus disk decomposition in [5,36,37] and are likely to overstate the contribution of the B/PS bulge itself.). Comparing B/T values between galaxies with and without X-shaped features, ref. [7] also found that the typical difference $\Delta[(B/T)_X - (B/T)_{no\ X}] \sim 0.1 - 0.2$ depending on the sample considered. For B/PS bulge sizes, refs. [4,33] found that boxy/peanut features typically extended up to about 0.2–0.5 of the bar size, with a median value around 0.4. Refs. [7,34]

measured the lengths of X-structure rays and found that they typically extend to about 1.2 disk scale lengths.

A distinctive characteristic of B/PS bulges, the angle between the X-structure rays and the disk plane, has also been measured in various studies. Using a sample of numerical models, ref. [20] showed that this angle evolves with time, decreasing as the bar grows. Its value also depends on the initial conditions in the disk and the dark matter halo, making it a valuable metric of a galaxy's secular evolution. Observational studies [33–35] find that X-structure angles range from 25° to 45° (the measurements from [33] can be converted to angles by taking the arctangent of b/a provided there), which is consistent with numerical results of [20], when the bar viewing angle is taken into account [35].

The primary focus of the present work is to expand our knowledge about the statistics of parameters of B/PS bulges (luminosity fraction, sizes, shapes, X-structure angles) and to compare those with what one obtains in up-to-date cosmological simulations like TNG50 for cosmological models. Compared to previous studies, where the B/PS bulges were either analyzed under the common roof of "pseudobulges" or only some geometric properties of such bulges were measured, here we want to analyze specially boxy/peanuts by means of 2D photometric decomposition, while separating the contribution of the B/PS bulges from other bulges (if present). This is in line with the studies of [30,31], which showed that bulges in disk galaxies can be composite structures, hosting multiple types of bulges and/or nuclear components, all of which contribute to the central intensity. This work can be considered a continuation of our previous observational studies of B/PS bulges, specifically [7,34,35], where B/PS bulges of real galaxies were analyzed through photometric decomposition. In the present study, we focus more on the sizes and contributions of B/PS bulges to the total intensity. Additionally, we perform a more sophisticated comparison between real and simulated galaxies than in [35], by converting the mass profiles of simulated galaxies into intensity maps in specific bandwidths using SKIRT (v9.0) [38,39] simulations.

The present work is structured as follows. In Section 2, we describe our EGIPS and Illustris TNG50 datasets and outline the procedure used to generate realistic images of TNG50 galaxies for different bar viewing angles with SKIRT. Section 3 presents an overview of our multicomponent photometric decomposition pipeline, in which the B/PS bulge is included as a separate component. In Section 4, we investigate the parameters of B/PS bulges obtained from the photometric decomposition and analyse their correlations with the properties of other structural components, such as the disk and additional bulges. Section 5 discusses our results in the context of previous studies of B/PS bulges and bar/bulge properties in TNG50. Finally, Section 6 summarises our conclusions.

2. Data

Two data sets were employed in the present study. The first consists of a subsample of galaxies taken from the Edge-on Galaxies in the Pan-STARRS survey (EGIPS, [40]). The Pan-STARRS survey is conducted with a 1.8 m telescope at Haleakalā Observatory (Hawaii) and covers the Northern Hemisphere, as well as part of the Southern Hemisphere down to Dec. = -30° deg. The data are available in five broad bands (g, r, i, z, y), with the resolution of 0.25 arcsec per pixel. Candidate galaxies for the present analysis were selected based on the outcomes of an automatic photometric decomposition conducted for each EGIPS galaxy in the i band (Savchenko et al., 2026, in prep., see https://www.sao.ru/edgeon/catalogs.php?cat=PS1cand1_imfit2). Specifically, galaxies hosting B/PS bulges were identified by the characteristic X-shaped patterns in the residuals, which were obtained by subtracting the photometric models of the disk and bulge from the original image. A similar technique was employed in [7] to identify galaxies with B/PS bulges in the DESI (Dark Energy

Spectroscopic Instrument) Legacy survey [41]. Galaxies exhibiting such residues were conveniently identified from the results of automatic decomposition, with a total number of 83 candidates. Subsequently, 12 galaxies were further excluded based on photometric decomposition results when the boxy or peanut-shaped features were deemed too weak, leaving a final sample of 71 galaxies with prominent B/PS bulges. Absolute magnitudes and spectroscopic distances (relative to the Cosmic Microwave Background, CMB) of selected galaxies are shown in Figure 1. Spectroscopic redshifts are compiled from the HyperLEDA (<http://atlas.obs-hp.fr/hyperleda/>) [42] and the NASA/IPAC Extragalactic Database (<https://ned.ipac.caltech.edu/>). Absolute magnitudes are taken from the EGIPS catalogue [40] and correspond to Kron magnitudes corrected for Galactic extinction [43]. In general, our sample consists of relatively bright galaxies, with a median absolute magnitude of $M_i = -21.3$ mag and a median distance of about 150 Mpc.

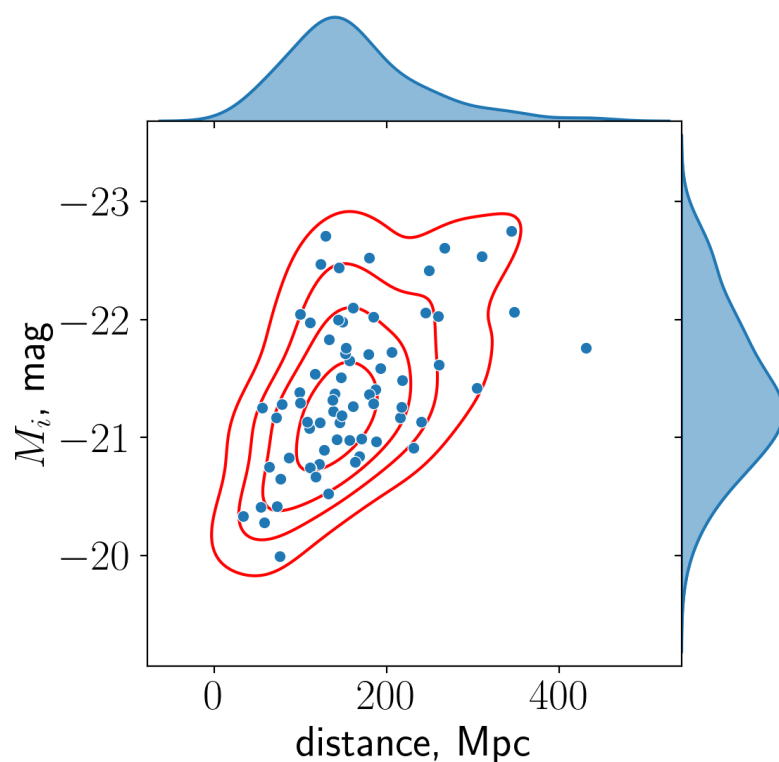


Figure 1. Redshift-derived spectroscopic distance versus absolute stellar magnitude in the i band for the sample of galaxies with boxy/peanut-shaped bulges, studied in the present work.

The second data set comprises cosmological Milky Way-like models, a sample compiled from Illustris TNG50 simulations by [44]. The sample consists of 198 relatively massive disk galaxies with stellar masses $M_*(r < 30 \text{ kpc}) = 10^{10.5-11.2} M_\odot$ and no massive companions; specifically, they do not have massive satellites $M_* > 10^{10.5} M_\odot$ within $r < 500 \text{ kpc}$ from the galactic center. For a detailed description of corresponding simulations, interested readers are referred to the original papers by [44,45]. Here, we should note that TNG50 is one of the most novel magnetohydrodynamic simulations, featuring the self-consistent evolution of dark matter, stars, gas, supermassive black holes, and magnetic fields, implemented through the AREPO code [46]. All these components are evolved from redshift $z = 127$ to $z = 0$ within a cubic volume of 51.7 Mpc (comoving units), with periodic boundaries. TNG50 benefits from a high spatial resolution, with galaxy models typically represented by about one million particles, and a softening length of around 300 pc at lower redshifts for star and dark matter particles. This resolution enables analysis of the vertical structure of galactic disks, as highlighted by [44].

Not all models from the sample of [44] host bars, and naturally, not all of them exhibit B/PS features when viewed edge-on (see also [47]). Therefore, the sample required additional processing. To obtain a sample of models with B/PS bulges, we prepared a preliminary set of images for each model, generated directly from the stellar mass distribution, featuring face-on and edge-on projections, which were then inspected visually. First, we selected models hosting bars (154 out of 198). Then, we rejected models that did not exhibit peanut features when viewed edge-on with the bar rotated perpendicularly to the LoS and/or the disk structure is significantly disturbed. This step cuts most of the sample by far, leaving only 56 cosmological models. Some candidates were further rejected after preliminary photometric decomposition, if the B/PS bulge photometric model were trying to account for prominent non-symmetric disk features, polar rings, etc. Our resulting sample of TNG50 galaxies consists of 20 models with prominent B/PS bulges.

To obtain realistic images of simulated galaxies, we employed the SKIRT radiative transfer code [38,39]. SKIRT is a versatile software tool capable of transforming three-dimensional simulation datasets into FITS images at specified wavelengths by incorporating the density distributions, softening lengths, and properties of stellar populations. These data are available directly from the TNG50 snapshots. To enable comparison with observational data, we prepared multiple images for each simulated galaxy in *i* band featuring different bar viewing angles, specifically, 90 deg, 50 deg, and 30 deg, to account for projection effects (see Figure 2). Additional simulations parameters are as follows:

1. TNG50 distances and masses are given in units of $h = H_0/100$, where H_0 is the Hubble constant. For example, masses are measured in units of $h^{-1}10^{10} M_\odot$. Those quantities were converted to appropriate values by dividing them by $h = 0.6774$.
2. Each galaxy is simulated in SKIRT using 10^9 photon packets.
3. Each image encompasses a region extending from -22.5 to 22.5 kpc from the galaxy center in the disk plane, and from -7.5 to 7.5 kpc along the vertical direction.
4. The images have a resolution of 300×100 pixels. The linear scale of each pixel is then 150 pc. Assuming a distance of 150 Mpc, this gives a pixel scale of 0.2 arcsec, which is slightly better than Pan-STARRS resolution.
5. Each stellar particle is assumed to represent a single stellar population, characterized by a Chabrier initial mass function [48], with defined formation time, metallicity, and the initial mass (mass at formation time). For the spectral energy distribution, we adopt the Bruzual and Charlot stellar population synthesis model [49].
6. As the smoothing length, we adopt the distance to the 32 nearest particles (see [50]), a parameter that is directly available in the TNG50 simulation snapshots. However, as noted in the SKIRT description (see https://skirt.ugent.be/root/_home.html), if the softening length is uncapped, it can lead to the appearance of large artificial blobs, as some distant particles in a given simulation snapshot can have very large distances (e.g., >100 kpc). Therefore, we capped the softening length at 1.5 kpc. In practice, we verified that the image does not change significantly as long as at least several pixels are covered by the softening length. For our chosen softening value, the softening covers 10 pixels.
7. The resulting images were convolved with a Gaussian kernel of FWHM 5 pixels (1 arcsec, assuming a distance of 150 Mpc), simulating the effect of the Pan-STARRS PSF in the *i*-band.

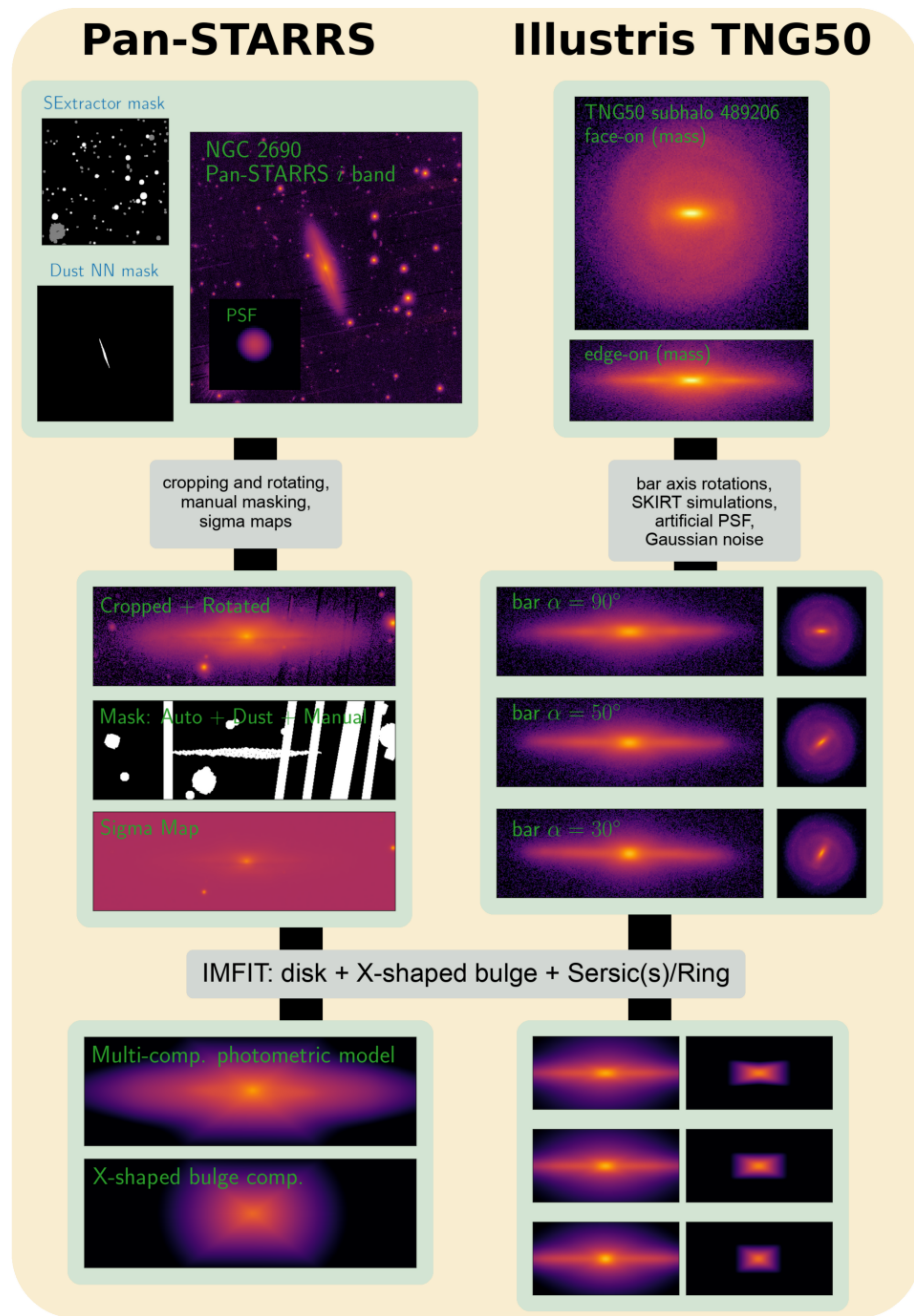


Figure 2. A general scheme of the galaxy processing pipeline used in the present work for EGIPS galaxies (**left side**) and Illustris TNG50 galaxies (**right side**).

3. Photometric Decomposition

3.1. Preprocessing

In this section we describe the image preparation for the photometric decomposition process (see Figure 2 for the illustration of the main steps). We start with the image cropping to obtain a field centered on the galaxy that fits the entire galaxy with margins of about the optical diameter of the galaxy. Next, to exclude the background objects from the analysis, we make a binary mask based on the objects catalogue produced by the SExtractor package [51] (the galaxy under consideration was excluded from the catalogue by its coordinates). When necessary we manually modified the mask to include image artifacts or extended features of oversaturated stars. In order to take into account the image smearing by the atmosphere and the telescope optics, we make PSF images. To do so we utilized the

PSFEX software package [52]. This package automatically extracts appropriate stars on a field based on a SExtractor catalogue and combines them into an output PSF image.

Since the dust attenuation can significantly impact the results of the decomposition [53], especially for highly inclined galaxies [54], we decided to mask regions close to a galactic disk plane, where the dust impact is most severe. To produce a dust mask we used a neural network model described in [54]. This model has a U-Net architecture [55] and was trained such that it takes a stack of g -, r -, and i -band images as an input and produces a binary mask that covers the regions most affected by dust (see [54] for more details). The dust masks obtained via the neural network were inspected visually and further modified manually if deemed necessary. Overall, the mask used during the decomposition process is a combined mask of background objects and dusty regions.

For the illustrative purposes we rotated the images to approximately align the disk plane with the x -axis.

3.2. General Setup

To obtain photometric models for our selected galaxies from EGIPS and synthetic images of cosmological models, we utilize the IMFIT software package (v1.8.0) [56]. Each image is fitted using a set of predefined 2D or 3D functions (see below). By default, IMFIT searches for the best-fit model by exploring the parameter space using the Levenberg–Marquardt algorithm [57]. However, since our models typically consist of at least three components, namely disk, B/PS bulge, and additional bulge and, thus, involve many parameters, we first run the Nelder–Mead simplex algorithm [58], which is slower but less prone to becoming trapped in local minima. After this initial step, we perform a more precise search using the Levenberg–Marquardt algorithm.

The best-fit parameters are found by minimising χ^2 statistics:

$$-2 \ln \mathcal{L} = \chi^2 = \sum_{i=0}^N w_i (I_{m,i} - I_{d,i})^2, \quad (1)$$

where \mathcal{L} is the likelihood of a given model, w_i are the pixel weights, and $I_{m,i}$ and $I_{d,i}$ are the intensities of the individual pixels in the photometric model and in the observed image, respectively. Weights w_i are reverse squares of Gaussian errors $w_i = 1/\sigma_i^2$, where

$$\sigma_i^2 = (I_{d,i}/g + \sigma_{\text{back}}^2). \quad (2)$$

g is the gain and σ_{back} is the standard deviation of the background, measured over 10^4 boxes of 10 arcsec size that are randomly distributed across the Pan-STARRS field of a galaxy. Note that errors in IMFIT are usually calculated based on the specified readnoise σ_{rdn} value, which we ignore here. This is because, in the course of this work, we found that readnoise values stored in Pan-STARRS data for corresponding galaxies do not accurately reflect the noise amplitude. For example, there are some cases where σ_{back} is two orders of magnitude greater than σ_{rdn} provided in the Pan-STARRS corresponding fields. We assume that the difference arises from the original background intensity, which was subsequently subtracted from the images by the Pan-STARRS pipeline, and, unfortunately, is unavailable for Pan-STARRS data. The use of σ_{back} in Equation (2) prevents the photometric model from fitting the noisy parts of the images that are underestimated by σ_{rdn} , while preserving the Poisson noise associated with the original data counts.

For our TNG50 images produced by SKIRT, we introduced Gaussian noise with the amplitude $\sigma = 0.03 \text{ MJy/sr}$ corresponding to the median value of background noise σ_{back} measured for our EGIPS sample and use the same χ^2 statistic described by Equation (1). We do not add Poisson noise to TNG50 images, since it is difficult to obtain proper ph-

ton counts estimate for Pan-STARRS images (see <https://outerspace.stsci.edu/spaces/PANSTARRS/pages/298812205/PS1+FAQ++Frequently+asked+questions>).

3.3. Photometric Functions

In course of this work, we assume that every galaxy image can be decomposed into a set of 2D functions, which we describe below.

The first one is the most commonly used in photometric studies, the Sérsic function [59]:

$$I(a) = I_e \exp \left[-\nu_n \left(\left(\frac{a}{r_e} \right)^{1/n} - 1 \right) \right], \quad (3)$$

where r_e is the effective radius (the radius containing half of the total flux), I_e is the brightness at r_e , n is the Sérsic index, ν_n is a function depending on n [60]. Note that a here is the elliptical radius, determined from the ellipticity of the isophotes ε and the pixel coordinates (x, y) as

$$a(x, y, \varepsilon) = \sqrt{x^2 + y^2 / (1 - \varepsilon)^2}. \quad (4)$$

We use Sérsic function primarily to describe an additional central structure that sometimes appears on top of the B/PS bulge. This component is usually smaller than the B/PS bulge and has rounder isophotes.

The disk is usually described by a 3D broken exponential profile:

$$j(R, z) = j_0 \operatorname{sech}^{2/n} \left(\frac{nz}{2z_d} \right) \times \begin{cases} \exp \left(-\frac{R}{h_1} \right), & R \leq R_T, \\ \exp \left(-\frac{R}{h_2} \right) \exp \left(\frac{R_T}{h_2} - \frac{R_T}{h_1} \right), & R > R_T, \end{cases} \quad (5)$$

where j_0 is the central luminosity density, z_0 is the vertical scale height, and n is the parameter describing how strongly the disk is concentrated in the vertical direction. The scale lengths h_1 and h_2 are the inner and outer radial scale lengths of the disk, respectively, and R_T is the location of the disk break. In some cases, a third scale h_3 (a double-broken profile) is introduced to describe an additional outer truncation of the surface-brightness profile in the galaxy outskirts. For the decompositions of edge-on galaxies with a B/PS bulge, the use of broken profiles often becomes a necessity. In fact, the break in the profile frequently represents an inner truncation, the existence of which is fully understandable from a dynamical point of view. Since a bar naturally forms from the disk material, a single exponential disk cannot extend all the way to the center; therefore, the profile must be modified to adequately represent real galactic disks. A similar model was used in [61] to describe the structure of CALIFA-DR3 (Calar Alto Legacy Integral Field Area Data Release 3) galaxies. However, in that work, the model was strictly two-dimensional (infinitesimal disk), whereas here, the luminosity density defined by (5) is integrated along the LoS to produce the proper disk image. By allowing the inclination to vary freely during fitting, we found that 75% of our EGIPS galaxies have an inclination greater than 85°, while the remaining 25% have inclinations between 75° and 85°. Also note that, to compare the sizes of B/PS bulges with the underlying disk sizes, we use an equivalent of disk scale lengths, defined as $h_{d,90} = R_{90}/3.89$ and $z_{d,90} = z_{90}/2.3$ (see Appendix A), where R_{90} is the radius containing 90% of the total disk intensity and z_{90} is the disk height containing 90% of the disk intensity, respectively.

To properly represent the B/PS bulges, we employ an X-shaped bulge function suggested in our previous work [35]. The model is a modified 2D Sérsic function with an exponential truncation added above the rays of X-structures:

$$I(x, y) = \begin{cases} I_S(x, y), & y \leq kx, \\ I_S(x_0, y) \cdot \exp(-|x - x_0|/s_X), & y > kx. \end{cases} \quad (6)$$

Here, $I_S(x, y)$ is the intensity of Sérsic 2D function (3), $\varphi = \arctan(k)$ describes the slope of the X-structure rays relative to the disk plane, and the coordinate x_0 is the abscissa of the point where the horizontal line (y) intersects the X-structure ray in a given quadrant. A schematic illustration of how the model intensity is calculated is presented in Figure 3. We also note that the model has been slightly updated compared to the version used in [35]: specifically, the intensity modifier in the bottom row of Equation (6) is now fixed at $I_S(x_0, y)$ instead of $I_S(x, y)$. Additional details are provided in Appendix B.

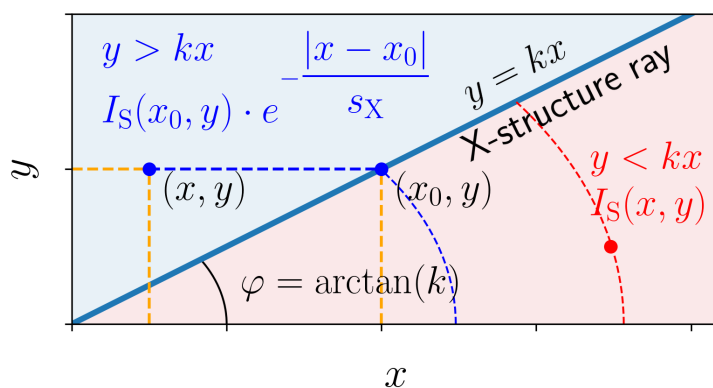


Figure 3. Schematic illustration of the intensity calculation in the X-shaped bulge photometric model used in the present study to represent the B/PS bulges of real and simulated galaxies. The figure is adapted from [35] with several modifications. The thick blue line indicates the X-structure ray; the light-red region marks the area below the ray, where the intensity is calculated following the standard Sérsic profile; the light-blue region marks the area above the ray, where the density truncation with the scale length s_X is introduced.

The X-shaped bulge function was thoroughly discussed in [35] and was tested on “naked” B/PS bulges of numerical models, which can be obtained by subtracting the disk from the galaxy using dynamical considerations (e.g., orbital frequencies), full models with the disk, and a sample of real galaxies. Essentially, this function introduces two additional parameters compared to the Sérsic function: the angle of the X-structure rays (φ) and scale length of the density decay from the ray along the horizontal direction towards the center (s_X). These parameters allow the model to describe a variety of morphologies, including the characteristic peanut shape, i.e., the gap between the rays (if present).

The X-shaped model offers an advantage over models based on generalized ellipses, which, while capable of modeling boxy isophotes, cannot properly reproduce the gap between the rays. However, we should note that our photometric function makes several simplifications, such as assuming that the X-structure rays are straight and relatively thin, and that the entire B/PS bulge has 4-fold symmetry about the galaxy center. In this study, as well as in our previous work, we also assume a Sérsic index of $n = 1$. This assumption simplifies the model and helps avoid potential degeneracies when other components, such as the classical bulges, are present in the galaxy center. While these assumptions are limitations of the model, trying to account for these complexities within the framework of photometric decomposition would require additional parameters to describe the B/PS

bulges. In practice, a model with only two extra parameters is already challenging to fit, as it requires an extensive search through the parameter space. Therefore, this model keeps a balance between simplicity and an adequate description of the B/PS bulge component.

Some additional notes are as follows. In the course of this work, we characterize B/PS bulges in terms of the ratio h_X/s_X , where by h_X we denote the scale length of the Sérsic part of Equation (6), i. e., the scale length of the profile below the X-structure ray. In practice, the ratio h_X/s_X indicates the degree of boxiness: small values correspond to horizontal isophotes above the ray (boxy), while large values correspond to sharp peanut-shaped profiles. The ellipticity is redefined as

$$\epsilon = \begin{cases} 1 - b/a, & b \leq a \\ a/b - 1, & b > a, \end{cases} \quad (7)$$

where a and b are the major and minor axes of an elliptical isophote. For $0 \leq \epsilon < 1$, this is the usual ellipticity, while values $\epsilon < 0$ correspond to elliptical isophotes elongated perpendicular to the disk. Specifically, $\epsilon = -1$ corresponds to vertical isophotes below the ray. This flexibility in defining ellipticity allows the model to properly reproduce boxy isophotes below the ray as well. Some examples of how the model looks depending on φ , h_X/s_X , and ϵ are provided in Figure 4.

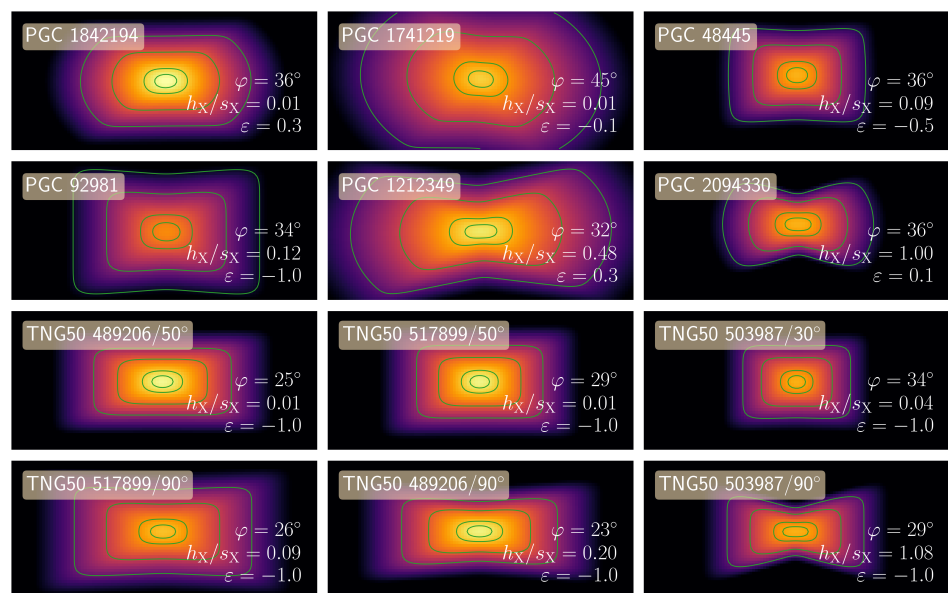


Figure 4. Examples of the best-fit model of the X-shaped bulge with different values of φ , h_X/s_X , and ϵ for selected galaxies from EGIPS and TNG50. Green contours represent the isophotes corresponding to 0.02, 0.1, 0.5, and 0.8 of the intensity maximum. For TNG50, the text following the backslash indicates the bar's viewing angle.

For galaxies with bright density enhancements in the disk plane and outside the B/PS bulge, we also employ a 3D Gaussian ring component:

$$j(r, z) = j(r_{\text{ring}}, 0) \exp\left(-\frac{(r - r_{\text{ring}})^2}{2\sigma_{\text{ring}}^2}\right) \exp\left(-\frac{|z|}{h_z}\right), \quad (8)$$

where r_{ring} is the ring radius, σ_{ring} is the ring thickness, h_z is the scale height, and $j(r_{\text{ring}}, 0)$ is the luminosity density at $r = r_{\text{ring}}$.

3.4. Fitting Essentials

For all galaxies in the sample and for the TNG50 cosmological models, we obtained suitable multi-component photometric models using the pipeline described above. In this subsection, we aim to provide the reader with an overview of how this was achieved and what steps were taken to assess the quality of the fits.

An example of the final fit, relative residuals, and images of the individual components for PGC 24926 (NGC 2690), a prominent galaxy with a B/PS bulge, are presented in Figure 5. To illustrate the improvement of the final model with the X-shaped bulge component compared to the simple disk plus Sérsic bulge decomposition, the figure also shows the corresponding photometric model from the original EGIPS run, its residuals, and images of both the disk and the bulge components in the top right corner. We prepared such comparative image collages for each galaxy in our sample as part of our decomposition routine to assess the quality of the fit (see the Supplementary Materials). Each collage was checked to ensure that the X-shaped structure in the residuals, if not entirely eliminated, became much less pronounced.

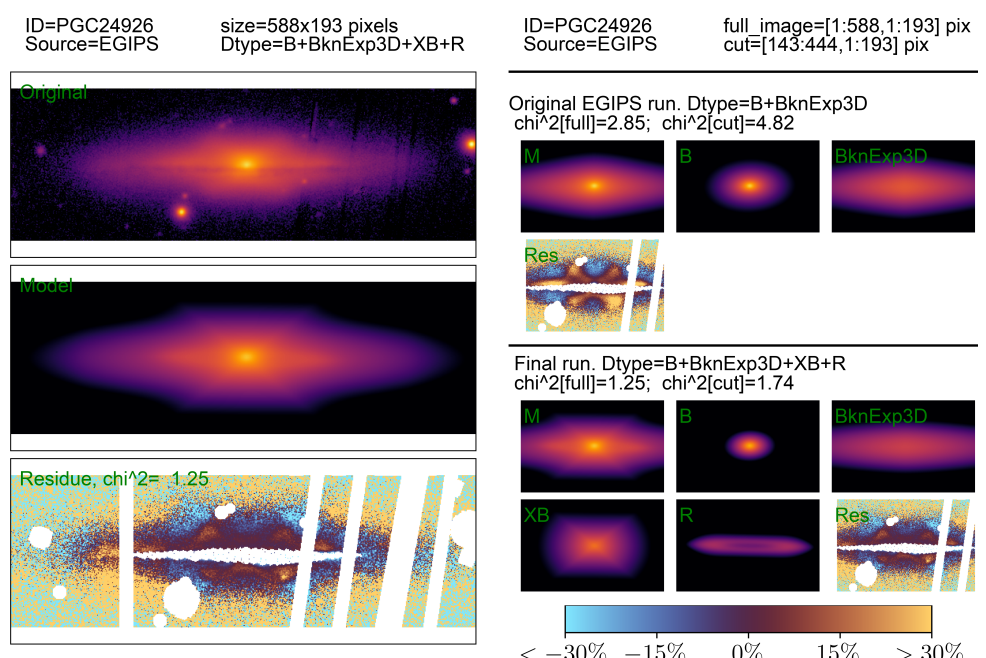


Figure 5. The photometric decomposition of PGC 24926 (NGC 2690). (Left): cropped and rotated Pan-STARRS *i*-band galaxy image (*top*), the best-fit photometric model (*middle*), and the residual image (*bottom*). (Right): the images of the individual photometric components and the residual image for the original EGIPS decomposition run with a simple Sérsic bulge (*top*) and decomposition performed in the present work with the X-shaped bulge model given by Equation (6) and a Gaussian ring (*bottom*). The auxiliary text above the images provides various details of the decomposition. The images in the right column show a smaller area where the B/PS bulge resides. Two chi-square values are provided in auxiliary text: one is calculated over all pixels used for the decomposition (“chi²[full]”) and the second one calculated over pixels from this smaller area (“chi²[cut]”). The latter is more sensitive to the residuals in the central area of the galaxy.

Figure 5 illustrates specific aspects of our study and the data as well. For example, note the vertical stripes that cross the image of the galaxy itself. These are artifacts from the Pan-STARRS dataset and were generally masked manually. The dust lane here is very prominent and rather thick, and it was also masked during the decomposition. The residual image from the bulge plus disk decomposition shows very prominent X-structures, which become much less pronounced in the final model. The residuals in the B/PS bulge region

are reduced to less than 10%. There is also a central bulge with a much smaller scale length than the B/PS bulge (3 arcsec vs. 9 arcsec, respectively) and about the same Sérsic index of $n = 1$. Additionally, there are density enhancements corresponding to either a ring or bar spurs, which appear in the residuals if no ring is included. The inclusion of the ring significantly reduces the residuals, as expected. Overall, as indicated in the legend of Figure 5, the model improves substantially, with the total χ^2 reduced by about three times, both for the entire image and for the central cut, where the B/PS bulge and the ring roughly reside.

Figure 6 compares the χ^2 statistics for all galaxies in our EGIPS sample between the original two-component decomposition (disk plus bulge) and our improved models for the central cut as well as the full galaxy image (see inset). The cut limits were determined visually and correspond to the central region of the galaxy where the B/PS bulge roughly resides (exact cut limits are provided in the corresponding collages for each galaxy in the Supplementary Materials). While the choice of limits is subjective, it provides a more sensitive metric for changes in the photometric model of the central component compared to the χ^2 calculated over the entire galaxy image. As can be seen from Figure 6, for all models, we indeed obtain a substantial improvement of the residue. Basically, almost all models end up with $1 \lesssim \chi^2 \lesssim 3$.

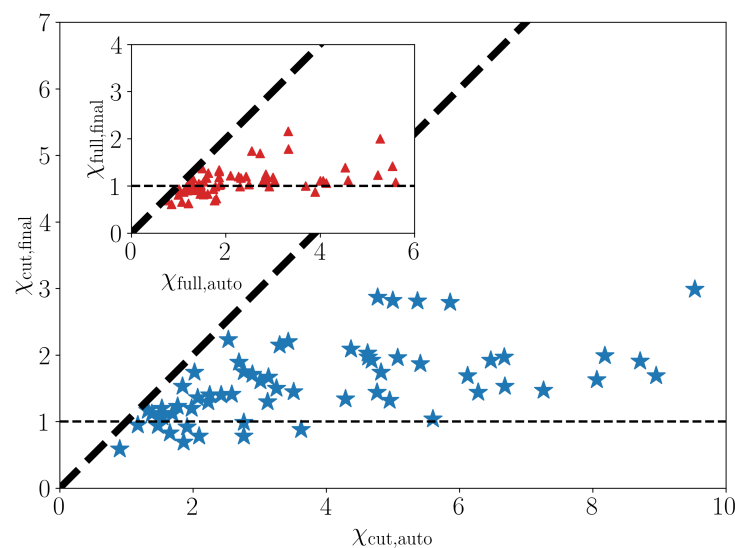


Figure 6. Comparison of the χ^2 statistic value from the original automatic EGIPS decomposition run with only bulge and disk components (y axis) and the multicomponent decomposition performed in the present work (x axis) for central area where the B/PS bulge resides (blue stars) and for the full galaxy image (inset, red triangles).

4. B/PS Bulge Parameters from Photometric Decomposition

In this section, we investigate the parameters of the B/PS bulges obtained for both the real galaxies from EGIPS and our TNG50 sample. We explore the possible correlations between the B/PS parameters and other structural parameters of galaxies, and also compare the parameters of real galaxies with those of the TNG50 models.

We mainly focus on the following physical quantities:

1. The X-structure opening angle φ . The angle value is generally linked to the dominant orbital family forming the B/PS bulge [28], which in turn is determined by the physical properties of the galaxy. However, it is also subject to projection effects, i.e., the orientation of the bar major axis with respect to the LoS [20,35].
2. The scale length of the Sérsic profile below the ray, which we denote as h_X to distinguish it from other scale lengths. Since we fixed Sérsic index to $n = 1$ for our X-shaped

bulge photometric model, h_X corresponds a simple exponential scale length. (note that r_e in Equation (3) is always the effective radius, even for $n = 1$. The corresponding exponential scale length h_X can be calculated as $r_e/1.678$). Its value generally tells us how large the B/PS bulge is.

3. Other geometric properties of the B/PS bulge: shape of isophotes below the ray ε and the amplitude of the intensity dip between the rays, quantified by h_X/s_X (see Section 3.3). In general, h_X/s_X may serve as an additional indicator of the bar viewing angle, with smaller values corresponding to a bar rotated closer to the LoS.

Median values of the parameters for each subsample discussed here are presented in Table 1 with the exception of h_X/s_X and ε , which, as we show below, tend to degenerate $h_X/s_X \rightarrow 0$ and $\varepsilon \rightarrow -1$, respectively. We also estimate the typical spread of values in each subsample as half of the interquartile range $(q_{75} - q_{25})/2.0$.

Table 1. Median values of the parameters for various photometric components for different subsamples considered in the present work. First column: the parameter under consideration, specifically, φ —the opening angle of X-structure rays; h_X —scale length of the B/PS bulge; $h_X/h_{d,90}$ —B/PS bulge scale length relative to the disk scale length $h_{d,90}$ (see Appendix A); $z_{d,90}$ —disk vertical scale length; $z_{d,90}/h_{d,90}$ —disk thickness; X/T —B/PS bulge-to-total luminosity ratio; X/D —B/PS bulge-to-disk luminosity ratio; B/T —contribution of other bulges (excluding the B/PS bulge) to the total luminosity; $(B + X)/T$ —total contribution of the central component (B/PS bulge plus other bulges). Columns from the second to fifth: median values and characteristic spread for EGIPS galaxies (second column) and TNG subsamples with different bar viewing angles (third to fifth columns, respectively). The spread of values (the values after the \pm sign) is estimated as half of the interquartile range, $(q_{75} - q_{25})/2.0$.

Parameter	EGIPS	TNG50 Bar 90°	Bar 50°	Bar 30°
φ , deg	37.13 ± 3.11	26.39 ± 1.46	30.64 ± 3.21	41.87 ± 7.21
h_X , kpc	1.10 ± 0.31	0.87 ± 0.13	0.74 ± 0.14	0.67 ± 0.13
$h_X/h_{d,90}$	0.26 ± 0.04	0.26 ± 0.07	0.22 ± 0.07	0.17 ± 0.04
$h_{d,90}$, kpc	4.45 ± 0.99	3.73 ± 0.68	4.07 ± 0.69	4.07 ± 0.79
$z_{d,90}$, kpc	0.93 ± 0.30	0.99 ± 0.21	0.99 ± 0.21	1.05 ± 0.23
$z_{d,90}/h_{d,90}$	0.23 ± 0.04	0.26 ± 0.07	0.25 ± 0.10	0.24 ± 0.08
X/T	0.22 ± 0.04	0.15 ± 0.07	0.17 ± 0.07	0.11 ± 0.07
X/D	0.36 ± 0.10	0.24 ± 0.13	0.32 ± 0.16	0.29 ± 0.11
B/T	0.08 ± 0.09	0.17 ± 0.06	0.16 ± 0.06	0.14 ± 0.07
$(B + X)/T$	0.34 ± 0.08	0.30 ± 0.11	0.31 ± 0.12	0.31 ± 0.10

4.1. X-Structure Angles and B/PS Bulge Sizes

Figure 7 shows the distributions and correlation plots of measured X-structure angles and the bulge scale length h_X , both in absolute values (kpc) and relative to the disk scale length $h_{d,90}$. As can be seen from the figure, the angles φ are mainly distributed between 30° and 50° for EGIPS galaxies. This range is consistent with previous works, both observational studies [34,35] and numerical simulations of isolated N-body galaxies [20]. The TNG50 galaxies are particularly interesting in terms of φ , as we measure very small angles $\varphi \sim 22^\circ - 23^\circ$ for some of them. It is difficult to estimate how many X-structures with such small angles are missed in observations due to selection effects, as smaller-angle X-structures are generally harder to detect. However, such small angles were not observed even in the isolated galaxy simulations from [20], where the smallest angle was 25°, found in the model with a substantial contribution from the non-baryonic component (dark halo) and at late stages of evolution ($t > 6$ Gyr).

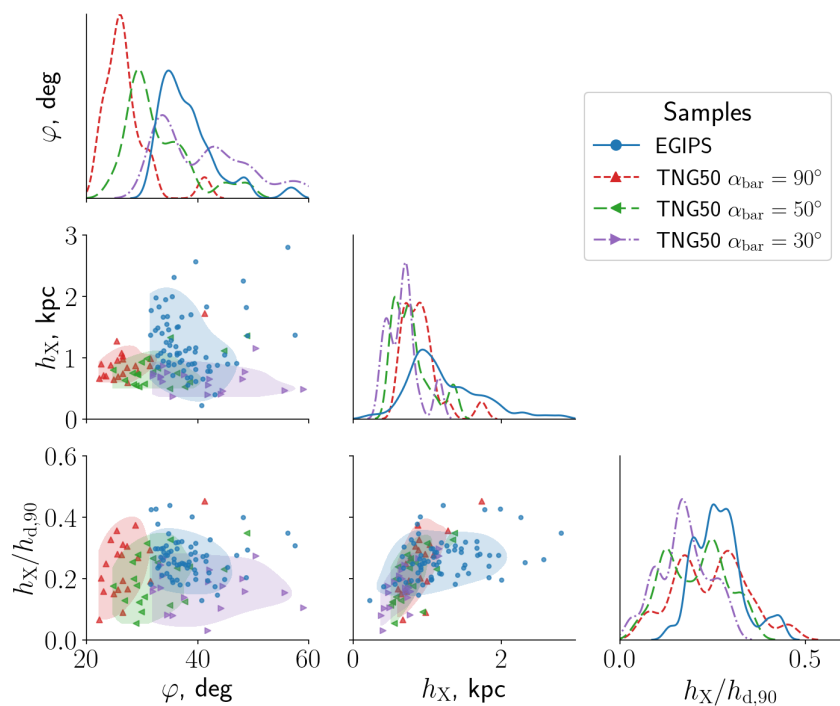


Figure 7. One-dimensional distributions of X-structure angles φ and B/PS bulge scale lengths h_X (in kpc and in units of the disk scale length $h_{d,90}$; diagonal panels), along with the corresponding correlation plots (off-diagonal panels), as measured from the photometric decomposition. Blue dots correspond to real galaxies from EGIPS sample, while red, green, and magenta triangles correspond to TNG50 subsamples with different bar viewing angles, 90° , 50° , and 30° , respectively. Filled contours enclose 75% of the respective subsamples.

The linear size subplots in Figure 7 (middle rows and columns) reveal several important trends. First, we observe that the higher the X-structure angle, the smaller the scale length of the bulge in general. One-dimensional distributions for different bar viewing angles in the TNG50 galaxies show that this dependency is a natural consequence of projection effects: the closer the bar is aligned with the LoS, the greater the X-structure angles is, and the smaller the bulge appears to be (see also Table 1).

Second, the linear scales for real galaxies span a range from approximately 0.3 kpc to 2.0 kpc. Comparing the scales of the TNG50 galaxies with our EGIPS sample, we see that the latter are generally larger. The peak of the one-dimensional distribution of real galaxies is clearly shifted toward greater values compare to TNG50 subsamples. In our TNG50 sample, there are almost no B/PS bulges with scales greater than 1.5 kpc. However, such bulges are present in real galaxies. We should note that the systematic absence of large bulges in our TNG50 sample due to selection effects is unlikely, since larger bulges are easier to distinguish. In terms of relative disk scales (third row and third column of Figure 7), the X-shaped bulges of real galaxies are also clearly larger, with the peak of the distribution occurring at around $h_X/h_{d,90} \sim 0.26$.

Figure 8 presents the cumulative distributions of isophotal parameters for X-shaped bulges: h_X/s_X (gap above the ray) and ε (isophotal profile below the ray). For the parameter h_X/s_X , we find that for most real galaxies and TNG50 models, this parameter tends to degenerate to $h_X/s_X \rightarrow 0$. This indicates that, for most of the studied galaxies and models, the isophotes above the rays are horizontal (boxy profile). For isophotes below the ray, we observe an interesting distinction between the bulges in TNG50 and EGIPS galaxies. In TNG50 galaxies, the isophotes are more flattened ($\varepsilon > 0$), while in EGIPS galaxies, the X-shaped bulges are characterized by more vertical isophotes ($\varepsilon < 0$).

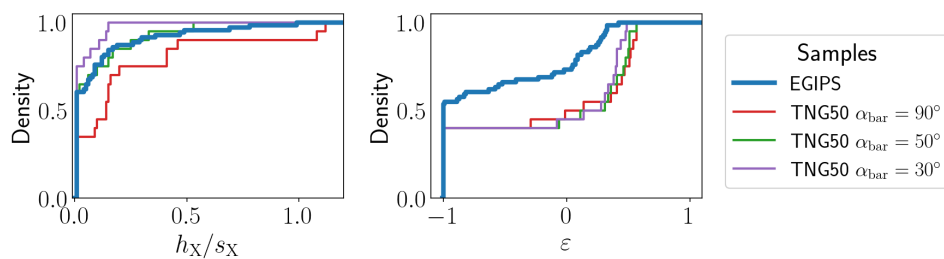


Figure 8. Cumulative distribution of isophotal parameters h_X/sx and ε of the B/PS bulges represented by a photometric model of the X-shaped bulge in EGIPS and TNG50 individual subsamples with different bar viewing angles. The color scheme follows that of Figure 7.

4.2. B/PS Bulge and Disk

Figure 9 presents the distributions of the measured disk scales, $h_{d,90}$ and $z_{d,90}$, as well as the disk thickness, and the dependence of the B/PS bulge parameters on these quantities. As the 1D distributions show (left column), the disk scale length of the EGIPS galaxies lies between 3 and 6 kpc for most of them. For the TNG50 galaxies, the scale lengths fall within the same range but are, on average, slightly smaller. Also note the slight shift of the scale length to larger values as the bar orientation moves closer to the LoS (see Table 1). For the disk thickness, the distribution peaks at $h_{d,90}/z_{d,90} \sim 0.23$, which is roughly consistent with the value measured by [62]. The disks of the measured TNG50 galaxies are generally slightly thicker, as they tend to have smaller $h_{d,90}$ while exhibiting approximately the same $z_{d,90}$.

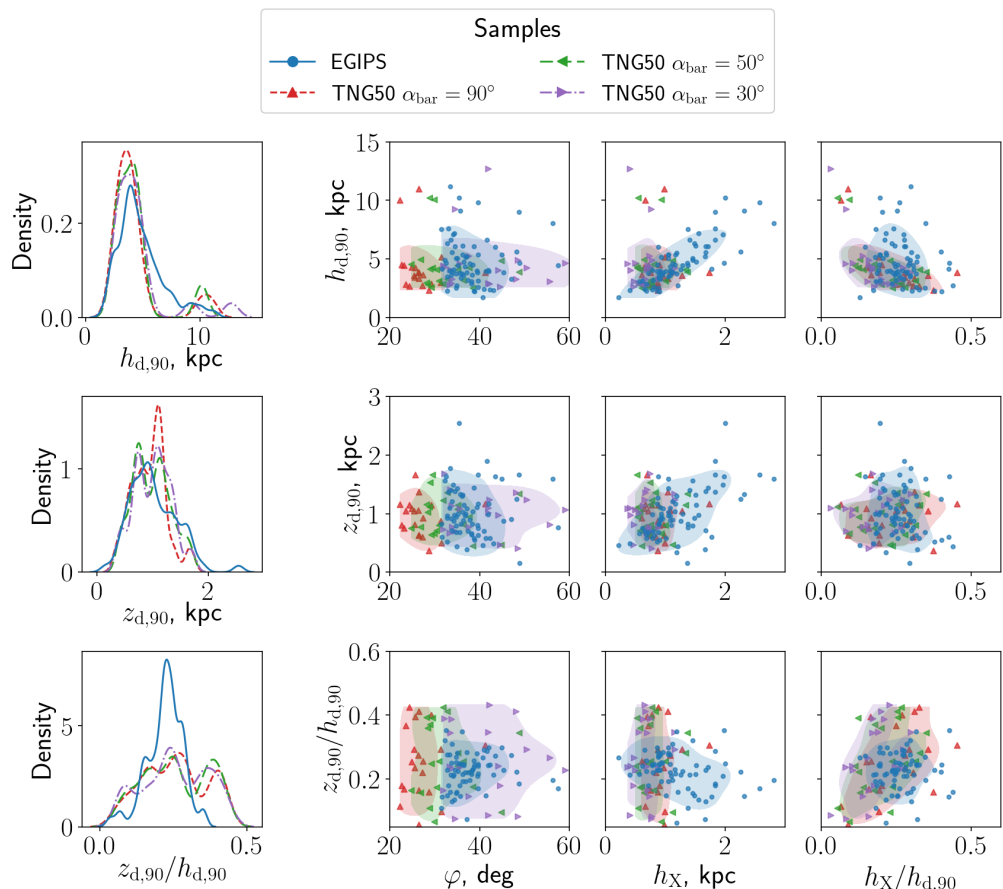


Figure 9. (Left): 1D distributions of disk scale lengths, in-plane (top) and vertical (middle), and disk thickness (bottom). (Second to fourth columns): disk scales (top and middle rows) and thickness (bottom row), depending on the X-structure angles (second column) and B/PS bulge scale lengths (in kpc and relative to the disk scale length, third and fourth columns, respectively). The color and symbol notation follows that of Figure 7.

Regarding the B/PS bulge parameters, we find that the angles do not show a clear dependence on either the linear scales or the disk thickness. At the same time, larger bulges are generally found in larger disks. It should be noted that in our previous numerical study of a variety of models [20], we found that the angle should depend on the disk thickness; however, we do not observe such a dependence here. It is difficult to pinpoint a clear reason for that; however, it should be noted that [20] compared the parameters of X-structures depending on the original parameters of the disk (i.e., at the start of simulations). It is quite possible that in observations we do not measure the same thickness, but rather the thickness of an already evolved disk, and therefore the dependence may no longer be apparent.

4.3. B/PS Bulge Intensity Contribution

Figure 10 presents the distributions of the B/PS bulge contribution to total intensity, denoted here as X/T (top row), relative to the disk only (X/D , second row), the contribution of other bulges B/T , calculated as a sum of all other Sérsic photometric components (e.g., $(B_1 + B_2)/T$ in the case of two additional bulges, third row), and the cumulative contribution of the B/PS bulge and other bulges $(X+B)/T$ (bottom row).

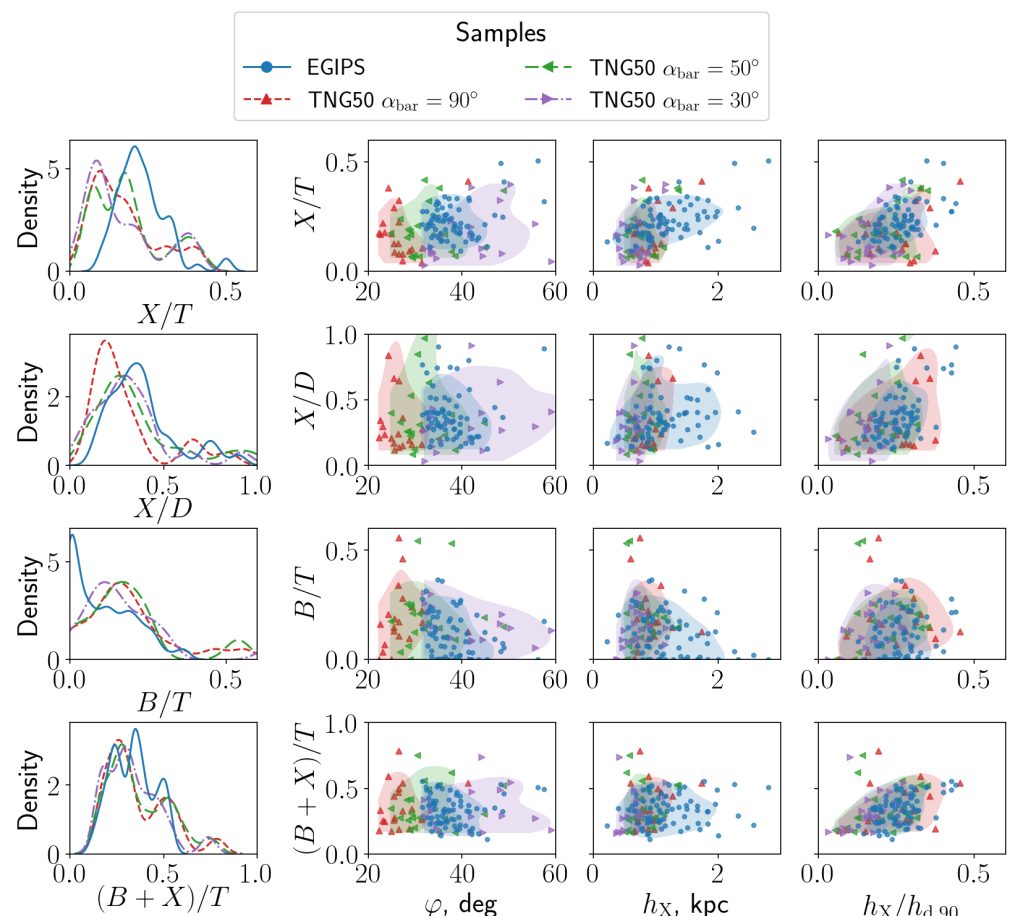


Figure 10. (Left): 1D distributions of B/PS bulge contribution to total intensity X/T (top row), relative to the disk only (X/D , second row), the contribution of other bulges B/T (third row), and the cumulative contribution of B/PS bulge and other bulges $(X+B)/T$ (bottom row). (Second to fourth columns): the parameters shown in the left column of each row, depending on the X-structure angles (second column) and B/PS bulge scale lengths (in kpc and relative to the disk scale length, third and fourth columns, respectively). The color and symbol notation follows that of Figure 7.

For X/D and X/T , we find that the B/PS bulges of real galaxies are generally more prominent compared to TNG50 galaxies (see also the values listed in Table 1). For X/D

in EGIPS galaxies, the median value is 0.35, which is consistent with the B/D values measured in [37] ($B/D \sim 0.3$), but appears to be larger than those measured in [5,34], where the median B/D values were smaller ($B/D \lesssim 0.2$). For $(B + X)/T$, we find that these cumulative values can be quite large (up to 0.5), with the median value $\mu_{(B+X)/T}$ around 0.3 for all subsamples.

Note that the contribution of other bulges (denoted B/T here) is, conversely, greater in TNG50 galaxies. For instance, comparing the median B/T value in EGIPS and TNG50 galaxies, where the bar is rotated perpendicular to LoS, $\mu(B/T)_{\text{EGIPS}} = 0.07$ and $\mu(B/T)_{\text{TNG50}} = 0.17$. This is qualitatively consistent with our observations during the decomposition of TNG50 galaxies. If the inner bulges are not adequately represented in their photometric model, the X-shaped bulge photometric model tends to degenerate into a standard 2D Sérsic profile. The B/T values of TNG50 galaxies are in good agreement with the values measured in [63], where the median measured value was $\mu(B/T) = 0.13$, based on 1D exponential plus Sérsic fits.

As for the dependencies of the B/PS bulge parameters on the disk, the only clear dependence is that X/T correlates with the size of the bulge (*top* row of Figure 10). Interestingly, we do not observe any dependence of the angles of X-structures on B/T values. In [20], we found that X-structures in galaxies with larger B/T , assuming B corresponds to the classical bulge, tend to be less flattened. However, Figure 10 does not support this conclusion.

5. Discussion

5.1. X-Structure Angles: Physics or Projection Effects?

One of the crucial questions in observational studies of B/PS bulges in general, and, naturally, in the present work, is what the observed angles of X-structures can tell us about the galaxies in which these angles are measured. On the one hand, simulation studies [20,28] show that the angles of X-structures are tightly connected with the orbital families that form the observed B/PS bulge. Because of this connection, the X-structure angles should depend on the overall gravitational potential of the system as well as on the bar properties. From [20], we know that the X-structure angles observed in side-on bars (bar viewing angle of 90°) vary from at least 25° to 40° , depending on physical factors such as bar age, the presence of a light or massive dark halo, and whether the bar forms from an initially thin or thick disk. On the other hand, the bar alignment with respect to the LoS strongly influences the distribution of the observed angles. As can be seen from Figure 7 and Table 1 for the TNG models, as well as from Figure 22 in [20], the typical shift in the X-structure angle between a bar viewed side-on and the same bar rotated to 30° is about 15° . This value is comparable to the intrinsic spread of angles found for strictly side-on bars across different N -body simulations.

Table 2 presents the Spearman rank correlation coefficients for the X-structure angles and various parameters and compares the correlations with our qualitative expectation from numerical study of [20] for such correlations. Specifically, we consider here the B/PS bulge scale lengths, both absolute and relative to the disk scale, the disk thickness, and B/PS bulge contribution both for EGIPS and TNG50 samples. We also investigate separately the correlation between the X-structure angles and the contribution of bulges with Sérsic index $n > 2$ for EGIPS, since [20] considered the impact of the classical bulges on the X-structures, rather than the pseudobulges. To facilitate comparison with observation data, we merged the results for TNG50 subsamples with different bar viewing angles here. We also separately considered a subsample of EGIPS galaxies, denoted as “EGIPS (cut)”, with measured disk inclinations $i > 80^\circ$ and moderate X-structure angles $\varphi < 45^\circ$. Basically,

the subsample formed this way should be more robust to possible errors, associated with resolution and disk inclination. The cut consists of 60 galaxies.

Table 2. Spearman rank correlation coefficients between measured X-structure angles and various parameters of the B/PS bulge, disk, and other bulges (first column) for EGIPS galaxies (second column), a cut of the EGIPS sample (third column; see the main text), and TNG50 models (fourth column). The statistically significant correlations (p -value < 0.05) are indicated in bold. In the fifth column, we present our qualitative expectations based on the results of previous studies on X-structures and B/PS bulges.

Parameter	EGIPS	EGIPS (Cut)	TNG50	Qualitative Expectations from Smirnov & Sotnikova (2018, [20])
$h_X/h_{d,90}$	−0.21	−0.29	−0.06	Strongly negative due to 1. bar viewing angles 2. secular bar growth
h_X , kpc	−0.30	−0.48	−0.17	Same as for $h_X/h_{d,90}$ but should additionally reflect the systematic trend of larger bars residing in more massive (larger) galaxies, see [64]
$z_{d,90}/h_{d,90}$	0.07	0.17	0.02	Positive, see Figure 16 in [20]
X/D	−0.10	−0.27	0.21	Negative due to the bar growth, ideally should be independent from the bar viewing angle
$B(n > 2)/T$	−0.17	−0.10	−	Positive, see Figure 16 in [20] and Figure 9 in [35]

In general, Table 2 highlights that there are no strong correlations or anti-correlations between X-structure angles and any of the considered parameters, except for the absolute B/PS bulge scale length h_X , even when we examine a subsample of galaxies selected by disk inclination and moderate X-structure angles. Let us discuss the correlations we can expect to observe for each of the considered parameters, based on our current understanding of B/PS bulges.

For $h_X/h_{d,90}$, one would expect a strong negative correlation due to projection effects (i.e., the B/PS bulge should appear smaller as the bar aligns closer to the LoS). Additionally, in numerical simulations, bars tend to slow down, grow in size over time, and their X-structures tend to flatten. The issue here is that no strong negative correlation is observed in the EGIPS sample. There is also no strong negative correlation in the TNG50 data. Figure 7 (left bottom subplot) gives a clue as to why this correlation may be absent. The figure shows that the intrinsic spread in B/PS bulge sizes plays a significant role, when estimating the correlations. For our TNG50 galaxies, the spread is large enough that it becomes comparable to the shift in median values due to bar viewing angles. For example, compare the intrinsic spread of values for bars observed perpendicular to the LoS in TNG50 $\Delta(h_X/h_{d,90}) = 0.07$ with the shift in the median value between TNG subsamples (see Table 1), $\mu(h_X/h_{d,90})_{\text{TNG } 90^\circ} = 0.26$ versus $\mu(h_X/h_{d,90})_{\text{TNG } 30^\circ} = 0.17$.

For absolute value of B/PS bulge sizes h_X we see a strong anti-correlation with X-structure angles. Figure 11 explains why the anti-correlation for absolute values of sizes can be stronger compared to relative sizes. Here, we plot the sizes of B/PS bulge, X-structure angles, and B/PS bulge intensity contribution depending on the absolute magnitude M_i of the galaxy in *i*-band (*top row*) and galaxy mass (*bottom row*) for our cut of the EGIPS sample. The masses of the galaxies were roughly estimated based on calibrations presented in [65]. Generally speaking, both M_i and the galaxy mass do not depend on the bar alignment to the LoS, and, thus, free of projection effects. In each individual subplot, we also show a value of the Spearman correlation coefficient r_s between the corresponding parameters and absolute magnitude M_i and the galaxy mass, respectively.

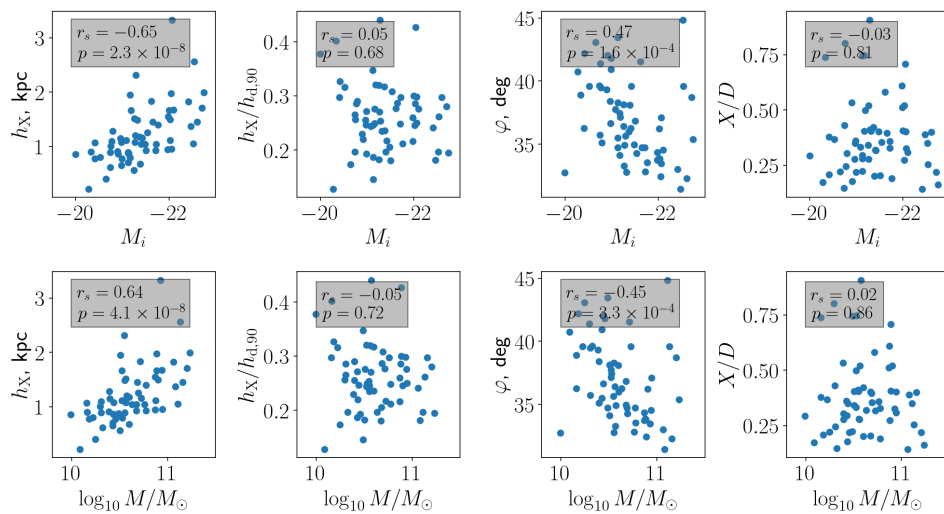


Figure 11. B/PS bulge scale length in kpc (**first column**), in units of the disk scale (**second column**), X-structure angles (**third column**), and B/PS bulge intensity contribution (**forth column**) depending on the absolute magnitude M_i (**top row**) and galaxy mass (**bottom row**), respectively. The Spearman correlation coefficient and the corresponding p -value are provided in a textbox in each corresponding subplot.

Figure 11 reveals several trends. First, the absolute sizes of B/PS bulges (*left column*) increase with galaxy mass, showing a significant positive correlation ($r_s \gtrsim 0.6$). This trend is consistent with two established facts: the number of B/PS bulges in observations sharply rises for galaxies with $M \gtrsim 10^{10.4} - 10.5$ [6,7], and the sizes of bars, from which B/PS bulges originate, also increase for galaxies with $M \gtrsim 10^{10.1}$ [64], being larger in more massive galaxies. The left column of Figure 11 shows that for galaxies with $M < 10^{10.4}$, B/PS bulges tend to be smaller, which may explain why they are more likely to be missed in B/PS bulge samples due to selection effects. On the other hand, larger bars should host larger B/PS bulges. Since larger bars are typically found in more massive galaxies, this would naturally imply that B/PS bulges in these galaxies should also be larger, which is supported by our measurements. However, neither the relative sizes of B/PS bulges (*second column* of Figure 11) nor their relative contribution to total intensity (*fourth column* of Figure 11) increase with galaxy mass. This absence of correlation suggests that, while B/PS bulges are larger in more massive galaxies, they are not necessarily older than those in less massive galaxies. If they were older, we would expect the relative sizes and intensity contributions to increase as well, which is not observed. Another trend, which has not been highlighted in previous B/PS bulge studies, is the moderate anti-correlation between X-structure angles and galaxy mass. As shown in the third column of Figure 11, X-structure angles tend to be smaller in more massive galaxies. While this result requires further testing with larger galaxy samples, it could suggest an intriguing distinction in the orbital dynamics of larger versus shorter bars.

For the other parameters, specifically the disk thickness and the bulge-to-total ratio, we observe a very weak positive correlation, while for the bulge-to-total ratio the correlation is weakly negative. However, both correlations have p -values above 0.05 and are therefore not statistically significant. We also emphasize that there are no bulges with $n > 2$ in our TNG50 sample (see also below); therefore, the corresponding correlation value is not included in the table. Regarding disk thickness, we note that the largest value examined in [20] was $z_d/h_d = 0.2$, whereas both EGIPS and TNG50 disks are generally thicker. Moreover, the model with $z_d/h_d = 0.2$ from [20] exhibited a prolonged buckling phase, while the B/PS bulges studied here do not show any strong asymmetry. This is likely due to the presence of additional bulge components, which tend to stabilise the bar against buckling [66]. In

short, direct comparison between [20] and either the EGIPS or TNG50 data is difficult in terms of disk thickness, as no models with $z_d/h_d \gtrsim 0.2$ were explored in that study. We conclude that further numerical studies, including models with thicker disks and with contributions from additional bulge components, are required for a proper investigations of trends in X-structure angles with disk thickness and other bulges contribution.

5.2. B/PS Bulges in TNG50

Here, we want to share some additional thoughts regarding B/PS bulges in Illustris TNG50 in light of the 2D photometric decomposition carried out in the present work.

First, as we showed in Section 4, the B/PS bulges in TNG50 galaxies are smaller than those in real galaxies, both in absolute terms and relative to the disk scale. These findings can be viewed from the perspective of the bar studies of TNG50 galaxies carried out so far. For example, ref. [67] found that bars in MaNGA [68] are larger than bars TNG50, and the corresponding sizes differ by about 50% in terms of the mean values. At the same time [69], showed that bars in TNG50 do not display the trend with galaxy mass that is observed in real galaxies. Since B/PS bulges originate from the corresponding bars, it is not surprising that our decomposition reveals that B/PS bulges are also smaller in TNG50. On the other hand, B/PS bulges in TNG50 galaxies show rather small X-structure angles when their bars are seen side-on. The problem is that, based on orbital studies of B/PS simulations carried out so far [28], we do not yet understand which properties of the overall gravitational potential could lead to the formation of X-structures with such small angles. Further orbital studies of bars in TNG50 may help to answer this question.

The second point concerns the other bulges, except B/PS bulges, in TNG50 and the overall decomposition of TNG50 galaxies. During this study, we found that TNG50 galaxies often have relatively bright central component(s) located within the central region of the B/PS bulge. Unless properly accounted for during the fitting, these central components make it impossible to fit the B/PS bulge model. This issue is reflected in Figure 10 and Table 1, where the contribution of other bulges, denoted as B/T , is found to be larger in TNG50 (see also the Supplementary Materials). This distinction may be related to the fact that we neglect the dust component when preparing the TNG50 galaxies images with SKIRT. Since the dust typically concentrates towards the galaxy center, it would likely decrease the intensity of the central component more than the disk contribution, leading to relatively smaller B/T . On the other hand, some studies [63] report that bulges with high Sérsic indexes ($n > 2$) are relatively rare in TNG50 galaxies, which is inconsistent with observational data. In the current study, we found that many central components of real galaxies exhibit Sérsic indexes $n > 2$ (see below), whereas the central components of TNG50 galaxies typically have $n \sim 1$ and even smaller. Since this study is purely photometric, identifying the reasons for these distinctions is beyond the scope of the present work. However, understanding them is crucial if we want to properly compare the structure of simulated and real galaxies.

5.3. B/PS Bulge as a Part of Composite Bulges

In most of our EGIPS galaxies, the central region is represented by a Sérsic component together with the X-shaped bulge component. In this sense, almost all of our bulges are composite, similar to the case of NGC 4565 described by [30], where a small inner bulge is found within the central part of a larger B/PS bulge. An important question regarding such composite bulges, emphasized by [30], is how the bulge properties inferred from a simple two-component (bulge + disk) decomposition compare with the properties of the central bulge obtained from a more sophisticated decomposition that explicitly includes the B/PS bulge as a separate component.

Figure 12 presents a comparison of the bulge-to-total ratio (B/T) and Sérsic indexes between two types of decomposition: the simple two-component decomposition (bulge + disk) from the original EGIPS run and our multicomponent decomposition, in which the B/PS bulge is included as a separate component. First, the figure shows that the B/T contribution typically becomes significantly smaller in the case of multicomponent decomposition, although the decrement varies from galaxy to galaxy. This is only natural to expect, considering that we effectively subtract the B/PS contribution to B/T in the multicomponent decomposition. Second, the central bulges in the multicomponent decomposition are generally more concentrated than those obtained in the two-component decomposition (middle panel of Figure 12). A comparison of the cumulative distributions of Sérsic indexes (right panel of Figure 12) illustrates this effect clearly: for example, only about 15% of bulges have $n > 4$ in the two-component decomposition, whereas this fraction increases to roughly 40% in the multicomponent case. Overall, Figure 12 emphasizes the importance of accounting for the composite structure of the bulges in photometric decomposition studies, since one can entirely miss which bulge (or other central components) the measured properties should be attributed to.

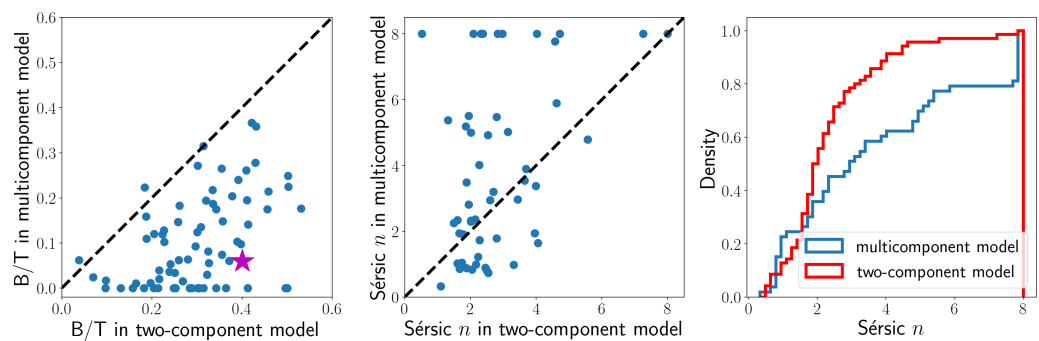


Figure 12. Comparison of bulge properties extracted from the automatic two-component decomposition (bulge + disk) of EGIPS galaxies and the multicomponent decomposition carried out in the present work. (Left): Bulge-to-total contributions B/T . The magenta star marks the values reported in [30] for NGC 4565. (Middle): Sérsic indexes n . (Right): Cumulative distribution of Sérsic indexes. Note that $n = 0.33$ and $n = 8$ are the limits imposed for the Sérsic component in the decomposition. In the (left) and (middle) subplots, the dashed line indicates the one-to-one correspondence.

6. Conclusions

In the present work, we studied the B/PS bulges of real galaxies from the EGIPS sample and a subsample of TNG50 galaxies with prominent B/PS bulges. In total, we considered 71 galaxies from EGIPS and 20 galaxies from TNG50. For the TNG50 galaxies, we prepared the images for three different bar viewing angles (90° , 50° , and 30°) using SKIRT simulations, adding Gaussian noise and convolving the resulting images with a PSF of 1 arcsec.

For each galaxy, we performed a 2D photometric decomposition of the corresponding images in the i -band and obtained a suitable photometric model (see the Supplementary Materials), where the B/PS bulge was accounted for separately from the disk and other bulges (if present) using our X-shaped bulge function introduced in [35] and further modified in the present work. In essence, the function is a modified 2D Sérsic profile, commonly used in photometric studies, but incorporating an exponential density decay above the X-structure rays. The model introduces two additional parameters compared to the standard Sérsic function: the scale length of the density decay above the ray, and the angle φ , which defines the inclination of the X-structure rays relative to the disk plane.

Studying the measured parameters of B/PS bulges and other components in the EGIPS galaxies and TNG50 models, we identified the following trends:

1. The X-structure angles are mostly distributed between 34° and 40° for real galaxies, whereas for TNG50 galaxies the angles span a range from about 22° to 45° , depending on the bar orientation with respect to the line of sight (smaller angles correspond to bars oriented perpendicular to the LoS); see Table 1. The values obtained for real galaxies are consistent with the results of previous observational and numerical studies. However, the very flat X-structures observed for TNG50 galaxies are inconsistent with the findings of previous numerical works. Further orbital studies of B/PS bulge in TNG50 galaxies are required to explain how such flat X-structures are formed.
2. The X-structure angles show a significant anti-correlation with the B/PS bulge size, that is, larger B/PS bulges tend to host more flattened X-structures (Table 2 and Figure 7). Comparing the B/PS bulges arising from bars viewed at different angles between the LoS and the bar major axis in the TNG50 models, we show that this effect is partially due to projection effects.
3. However, when examining the B/PS bulge sizes and X-structure angles against the absolute magnitudes and galaxy masses of real galaxies, quantities that are independent of the bar viewing angle, we found that both larger B/PS bulges and more flattened X-structures tend to reside in more massive galaxies (Figure 11). This suggests that the observed negative correlation between B/PS bulge size and X-structure angle is not solely a projection effect but also has a physical origin. The trend of larger bulges residing in more massive galaxies is consistent with previous findings that larger bars are found in more massive galaxies. The trend of more flattened X-structures residing in larger B/PS bulges (and, thus, in larger bars) is a new finding of the present work. These results should be further tested with a larger sample of galaxies with B/PS bulges.
4. The measured contributions of the B/PS bulge and other bulges to total intensity are consistent with the results of previous studies where automatic decomposition was employed. At the same time, larger B/PS bulges are typically found in larger disks, and generally have larger the bulge-to-total intensity ratio, X/T (Figure 10).
5. When studying the dependence of X-structure angles on disk parameters and the contribution of other bulges, B/T , we did not find any significant correlations (Table 2).
6. Comparing the B/PS bulges between EGIPS galaxies and the TNG50 models, we find that the B/PS bulges of real galaxies are considerably larger (see h_X parameter values in Table 1), both in absolute terms and relative to the disk scale. This is consistent with previous studies of TNG50 bars, which have shown that they are shorter than the bars of real galaxies. At the same time, we find that B/PS bulges in TNG50 are generally less prominent in terms of their intensity-to-total ratio, X/T , compared to real galaxies (see Table 1).
7. Comparing the results between a simple bulge + disk decomposition and our multicomponent decomposition, we find that accounting for the B/PS bulge separately is essential for obtaining realistic estimates of the bulge-to-total ratio, B/T . We also found that the bulges extracted by the two-component model tend to have smaller Sérsic indices compared to the case where the B/PS bulge is properly accounted for (Figure 12).

In general, we want to emphasize that our study is the first to analyze such a large sample of real and model edge-on galaxies hosting B/PS bulges using the same 2D photometric decomposition approach. Unfortunately, B/PS bulges are objects for which the observable properties are strongly influenced by the bar viewing angle. However, as highlighted in this work, their properties can still be examined in relation to global galaxy properties that are independent of the bar viewing angle, thus providing valuable insights into the actual vertical structure of the bars.

Supplementary Materials: The images of photometric models of all galaxies and TNG models considered in this study can be downloaded at: <https://www.mdpi.com/article/10.3390/galaxies1010000/s1>.

Author Contributions: Conceptualization, Anton Smirnov, Alexander Marchuk and Natalia Sotnikova; Methodology, Anton Smirnov and Alexander Marchuk; Software, Anton Smirnov; Validation, Anton Smirnov; Formal analysis, Anton Smirnov and Alexander Marchuk; Investigation, Anton Smirnov; Resources, Anton Smirnov and Sergey Savchenko; Data curation, Anton Smirnov, Alexander Marchuk and Sergey Savchenko; Writing – original draft, Anton Smirnov; Writing – review & editing, Anton Smirnov, Alexander Marchuk, Viktor Zozulia, Natalia Sotnikova and Sergey Savchenko; Visualization, Anton Smirnov, Alexander Marchuk and Viktor Zozulia; Supervision, Natalia Sotnikova.

Funding: The authors acknowledge financial support from the Russian Science Foundation, grant no. 24-22-00376.

Data Availability Statement: The original contributions presented in this study are included in the article/supplementary material. Further inquiries can be directed to the corresponding author(s).

Acknowledgments: This research has made use of the NASA/IPAC Extragalactic Database (NED), which is operated by the Jet Propulsion Laboratory, California Institute of Technology, under contract with the National Aeronautics and Space Administration.

Conflicts of Interest: The authors declare no conflicts of interest.

Appendix A. Broken Disk in the Framework of 2D Decomposition

Since we use the broken disk model, which is not frequently applied to describe edge-on galaxies, we provide here some clarifications on how the model works for our galaxies. The first point to note is that it is common for the inner disk scale length to approach infinity during the fitting $h_{\text{inner}} \rightarrow \infty$. In practice, it was fixed at a constant value once it exceeded the other scale lengths by an order of magnitude. Physically, a large inner scale length implies a plateau in the central intensity distribution of the disk. Of course, this is a rather rough approximation of the true density distribution of the disk, since the bar forms from the disk's stellar material. However, we believe that even a plateau is more physically reasonable than assuming that a single exponential disk extends all the way to the center. Therefore, we decided to keep it as is, rather than artificially constraining the inner scale length to some small fixed value.

Secondly, because we use the broken disk model, it is not straightforward to choose the “correct” scale length among several possible values. Therefore, in this work, we adopt the quantity $h_{d,90}$ defined as $R_{90}/3.89$, where R_{90} is the cylindrical radius enclosing 90% of the disk (not total!) intensity. For a pure exponential disk, this quantity equals the disk scale length. For disks with multiple scale lengths, it provides an estimate of the characteristic disk size. Since we observe the galaxies in edge-on position, R_{90} cannot be calculated directly from the disk image due to projection effects. Instead, we calculate it from the density profile (Equation (5)) by integrating it along the cylindrical radius. R_{90} is then determined by comparing the integral value from zero to infinity with that from zero to a specific radius R .

For the disk thickness, a similar issue arises. The vertical disk profile is described by $\text{sech}^{2/n}[nz/(2z_d)]$ and depends on n . Therefore, the ratio z_d/h_d does not strictly measure the disk thickness. To study how the parameters of X-shaped bulges depend on the disk thickness, we introduce the quantity $z_{d,90} = z_{90}/2.3$, where z_{90} is defined as the height that contains 90% of the total disk intensity. This is measured by integrating the vertical profile with a given n value and comparing the intensity within the layer $[0, z]$ to the integral from zero to infinity. For a pure exponential profile, $z_{d,90} = 2.3z_d$. For other profiles, the ratio $z_{d,90}/h_{d,90}$ can be used as an estimate of the disk thickness.

Appendix B. X-Shaped Bulge Model Additional Notes

Here, we provide a detailed explanation of why we use the modifier $I_S(x_0, y)$ in the bottom row of Equation (6), instead of $I_S(x, y)$ as used in [35].

There are two reasons for introducing this modification. First, it prevents the model from increasing the intensity above the rays in the vertical direction. This was possible in the original formulation because, while the intensity decreases as one moves from the ray toward the center due to the introduced cutout, the intensity of the base Sérsic profile increases. The interaction of these two factors could lead to unrealistic solutions in the case of slightly inclined disks if the model attempted to account for the intensity of the inclined disk.

Secondly, having two counteracting factors in the intensity modifier hurts the transparency in the interpretation of the model parameters, since the amplitude of the intensity dip then depends on both s_X and the ellipticity of the isophotes of the base Sérsic profile ε . In particular, in [35], we suggested that the ratio of the base Sérsic scale length to the scale length of the density truncation, h_X/s_X , can be used as a measure of the intensity dip alone. However, in the original formulation, in case of vertical isophotes below the ray ($\varepsilon = -1$), $h_X/s_X = 1$ actually means horizontal isophotes above the ray, since the increases and decreases compensate each other. On the other hand, for $\varepsilon = 0.4 - 0.5$, $h_X/s_X = 1$ corresponds to a very prominent intensity dip between the rays. Generally, the intensity dip can be parameterized as the ratio of intensities at the center and along the ray, measured along the same horizontal line. For example:

$$I(0, kh_X) / I(h_X, kh_X) = \exp(-h_X/s_X) \quad (\text{A1})$$

for the model defined by Equation (6). In the case of the original model from [35], however:

$$I(0, kh_X) / I(h_X, kh_X) = \exp(-k/\varepsilon - h_X/s_X + \sqrt{1 + k^2/\varepsilon^2}), \quad (\text{A2})$$

where ε is the usual axis ratio b/a and $k = \tan \varphi$. In the limit $\varepsilon \rightarrow \inf$ (i.e., $b \gg a$), we have $I(0, kh_X) / I(h_X, kh_X) \rightarrow \exp(1 - h_X/s_X)$. In other words, when $b \gg a$, $h_X/s_X = 1$ corresponds to the case with no density dip between the rays, $I(0, kh_X) / I(h_X, kh_X) = 1$.

This was not clear in [35], since the X-shaped bulges of the simulated galaxies used to formulate the model exhibit a clear density dip between the rays and similar isophote ellipticity values. Now, in the updated version described by Equation (6), the density dip is properly measured by the ratio h_X/s_X alone.

References

- Shaw, M.A. The nature of 'box' and 'peanut' shaped galactic bulges. *Mon. Not. R. Astron. Soc.* **1987**, *229*, 691–706. <https://doi.org/10.1093/mnras/229.4.691>.
- de Souza, R.E.; Dos Anjos, S. Box-shaped galaxies: A complete list. *Astron. Astrophys. Suppl. Ser.* **1987**, *70*, 465–480.
- Lütticke, R.; Dettmar, R.J.; Pohlen, M. Box- and peanut-shaped bulges. I. Statistics. *Astron. Astrophys. Suppl. Ser.* **2000**, *145*, 405–414. <https://doi.org/10.1051/aas:2000354>.
- Erwin, P.; Debattista, V.P. Peanuts at an angle: Detecting and measuring the three-dimensional structure of bars in moderately inclined galaxies. *Mon. Not. R. Astron. Soc.* **2013**, *431*, 3060–3086. <https://doi.org/10.1093/mnras/stt385>.
- Yoshino, A.; Yamauchi, C. Box/peanut and bar structures in edge-on and face-on nearby galaxies in the Sloan Digital Sky Survey—I. Catalogue. *Mon. Not. R. Astron. Soc.* **2015**, *446*, 3749–3767. <https://doi.org/10.1093/mnras/stu2249>.
- Erwin, P.; Debattista, V.P. The frequency and stellar-mass dependence of boxy/peanut-shaped bulges in barred galaxies. *Mon. Not. R. Astron. Soc.* **2017**, *468*, 2058–2080. <https://doi.org/10.1093/mnras/stx620>.
- Marchuk, A.A.; Smirnov, A.A.; Sotnikova, N.Y.; Bunakalya, D.A.; Savchenko, S.S.; Reshetnikov, V.P.; Usachev, P.A.; Tikhonenko, I.S.; Zozulia, V.D.; Zakharova, D.A. B/PS bulges in DESI Legacy edge-on galaxies—I. Sample building. *Mon. Not. R. Astron. Soc.* **2022**, *512*, 1371–1390. <https://doi.org/10.1093/mnras/stac599>.
- Pfenniger, D.; Friedli, D. Structure and dynamics of 3D N-body barred galaxies. *Astron. Astrophys.* **1991**, *252*, 75–93.

9. Skokos, C.; Patsis, P.A.; Athanassoula, E. Orbital dynamics of three-dimensional bars—I. The backbone of three-dimensional bars. A fiducial case. *Mon. Not. R. Astron. Soc.* **2002**, *333*, 847–860. <https://doi.org/10.1046/j.1365-8711.2002.05468.x>.
10. Combes, F.; Sanders, R.H. Formation and properties of persisting stellar bars. *Astron. Astrophys.* **1981**, *96*, 164–173.
11. Raha, N.; Sellwood, J.A.; James, R.A.; Kahn, F.D. A dynamical instability of bars in disk galaxies. *Nature* **1991**, *352*, 411. <https://doi.org/10.1038/352411a0>.
12. Athanassoula, E.; Misiriotis, A. Morphology, photometry and kinematics of N-body bars—I. Three models with different halo central concentrations. *Mon. Not. R. Astron. Soc.* **2002**, *330*, 35–52. <https://doi.org/10.1046/j.1365-8711.2002.05028.x>.
13. O’Neill, J.K.; Dubinski, J. Detailed comparison of the structures and kinematics of simulated and observed barred galaxies. *Mon. Not. R. Astron. Soc.* **2003**, *346*, 251–264. <https://doi.org/10.1046/j.1365-2966.2003.07085.x>.
14. Athanassoula, E. On the nature of bulges in general and of box/peanut bulges in particular: Input from N-body simulations. *Mon. Not. R. Astron. Soc.* **2005**, *358*, 1477–1488. <https://doi.org/10.1111/j.1365-2966.2005.08872.x>.
15. Martinez-Valpuesta, I.; Shlosman, I.; Heller, C. Evolution of Stellar Bars in Live Axisymmetric Halos: Recurrent Buckling and Secular Growth. *Astrophys. J.* **2006**, *637*, 214–226. <https://doi.org/10.1086/498338>.
16. Debattista, V.P.; Mayer, L.; Carollo, C.M.; Moore, B.; Wadsley, J.; Quinn, T. The Secular Evolution of Disk Structural Parameters. *Astrophys. J.* **2006**, *645*, 209–227. <https://doi.org/10.1086/504147>.
17. Wozniak, H.; Michel-Dansac, L. Formation of young boxy/peanut bulges in ringed barred galaxies. *Astron. Astrophys.* **2009**, *494*, 11–20. <https://doi.org/10.1051/0004-6361:200810903>.
18. Saha, K.; Gerhard, O. Secular evolution and cylindrical rotation in boxy/peanut bulges: Impact of initially rotating classical bulges. *Mon. Not. R. Astron. Soc.* **2013**, *430*, 2039–2046. <https://doi.org/10.1093/mnras/stt029>.
19. Frakoudi, F.; Di Matteo, P.; Haywood, M.; Gómez, A.; Combes, F.; Katz, D.; Semelin, B. Bars and boxy/peanut bulges in thin and thick discs. I. Morphology and line-of-sight velocities of a fiducial model. *Astron. Astrophys.* **2017**, *606*, A47. <https://doi.org/10.1051/0004-6361/201630244>.
20. Smirnov, A.A.; Sotnikova, N.Y. What determines the flatness of X-shaped structures in edge-on galaxies? *Mon. Not. R. Astron. Soc.* **2018**, *481*, 4058–4076. <https://doi.org/10.1093/mnras/sty2423>.
21. Sellwood, J.A.; Gerhard, O. Three mechanisms for bar thickening. *Mon. Not. R. Astron. Soc.* **2020**, *495*, 3175–3191. <https://doi.org/10.1093/mnras/staa1336>.
22. Bureau, M.; Freeman, K.C. The Nature of Boxy/Peanut-Shaped Bulges in Spiral Galaxies. *Astron. J.* **1999**, *118*, 126–138. <https://doi.org/10.1086/300922>.
23. Chung, A.; Bureau, M. Stellar Kinematics of Boxy Bulges: Large-Scale Bars and Inner Disks. *Astron. J.* **2004**, *127*, 3192–3212. <https://doi.org/10.1086/420988>.
24. Kruk, S.J.; Erwin, P.; Debattista, V.P.; Lintott, C. Revealing the cosmic evolution of boxy/peanut-shaped bulges from HST COSMOS and SDSS. *Mon. Not. R. Astron. Soc.* **2019**, *490*, 4721–4739. <https://doi.org/10.1093/mnras/stz2877>.
25. Patsis, P.A.; Xilouris, E.M.; Alikakos, J.; Athanassoula, E. Edge-on boxes with X-features as parts of galactic bars. NGC 352: A direct piece of observational evidence. *Astron. Astrophys.* **2021**, *647*, A20. <https://doi.org/10.1051/0004-6361/202039570>.
26. Patsis, P.A.; Katsanikas, M. The phase space of boxy-peanut and X-shaped bulges in galaxies—I. Properties of non-periodic orbits. *Mon. Not. R. Astron. Soc.* **2014**, *445*, 3525–3545. <https://doi.org/10.1093/mnras/stu1988>.
27. Portail, M.; Wegg, C.; Gerhard, O. Peanuts, brezels and bananas: Food for thought on the orbital structure of the Galactic bulge. *Mon. Not. R. Astron. Soc.* **2015**, *450*, L66–L70. <https://doi.org/10.1093/mnrasl/slv048>.
28. Parul, H.D.; Smirnov, A.A.; Sotnikova, N.Y. Orbital Ingredients for Cooking X-structures in Edge-on Galaxies. *Astrophys. J.* **2020**, *895*, 12. <https://doi.org/10.3847/1538-4357/ab76ce>.
29. Kormendy, J.; Kennicutt, R.C., Jr. Secular Evolution and the Formation of Pseudobulges in Disk Galaxies. *Annu. Rev. Astron. Astrophys.* **2004**, *42*, 603–683. <https://doi.org/10.1146/annurev.astro.42.053102.134024>.
30. Kormendy, J.; Barentine, J.C. Detection of a Pseudobulge Hidden Inside the “Box-shaped Bulge” of NGC 4565. *Astrophys. J. Lett.* **2010**, *715*, L176–L179. <https://doi.org/10.1088/2041-8205/715/2/L176>.
31. Erwin, P.; Seth, A.; Debattista, V.P.; Seidel, M.; Mehrgan, K.; Thomas, J.; Saglia, R.; de Lorenzo-Cáceres, A.; Maciejewski, W.; Fabricius, M.; et al. Composite bulges—II. Classical bulges and nuclear discs in barred galaxies: The contrasting cases of NGC 4608 and NGC 4643. *Mon. Not. R. Astron. Soc.* **2021**, *502*, 2446–2473. <https://doi.org/10.1093/mnras/stab126>.
32. Ciambur, B.C.; Graham, A.W. Quantifying the (X/peanut)-shaped structure in edge-on disc galaxies: Length, strength, and nested peanuts. *Mon. Not. R. Astron. Soc.* **2016**, *459*, 1276–1292. <https://doi.org/10.1093/mnras/stw759>.
33. Laurikainen, E.; Salo, H. Barlenses and X-shaped features compared: Two manifestations of boxy/peanut bulges. *Astron. Astrophys.* **2017**, *598*, A10. <https://doi.org/10.1051/0004-6361/201628936>.
34. Savchenko, S.S.; Sotnikova, N.Y.; Mosenkov, A.V.; Reshetnikov, V.P.; Bizyaev, D.V. Measuring the X-shaped structures in edge-on galaxies. *Mon. Not. R. Astron. Soc.* **2017**, *471*, 3261–3272. <https://doi.org/10.1093/mnras/stx1802>.
35. Smirnov, A.A.; Savchenko, S.S. New X-shaped bulge photometric model as a tool for measuring B/PS bulges and their X-structures in photometric studies. *Mon. Not. R. Astron. Soc.* **2020**, *499*, 462–481. <https://doi.org/10.1093/mnras/staa2892>.

36. Simard, L.; Mendel, J.T.; Patton, D.R.; Ellison, S.L.; McConnachie, A.W. A Catalog of Bulge+disk Decompositions and Updated Photometry for 1.12 Million Galaxies in the Sloan Digital Sky Survey. *Astrophys. J. Suppl. Ser.* **2011**, *196*, 11. <https://doi.org/10.1088/0067-0049/196/1/11>.

37. Bizyaev, D.V.; Kautsch, S.J.; Mosenkov, A.V.; Reshetnikov, V.P.; Sotnikova, N.Y.; Yablokova, N.V.; Hillyer, R.W. The Catalog of Edge-on Disk Galaxies from SDSS. I. The Catalog and the Structural Parameters of Stellar Disks. *Astrophys. J.* **2014**, *787*, 24. <https://doi.org/10.1088/0004-637X/787/1/24>.

38. Baes, M.; Verstappen, J.; De Looze, I.; Fritz, J.; Saftly, W.; Vidal Pérez, E.; Stalevski, M.; Valcke, S. Efficient Three-dimensional NLTE Dust Radiative Transfer with SKIRT. *Astrophys. J. Suppl. Ser.* **2011**, *196*, 22. <https://doi.org/10.1088/0067-0049/196/2/22>.

39. Camps, P.; Baes, M. SKIRT: An advanced dust radiative transfer code with a user-friendly architecture. *Astron. Comput.* **2015**, *9*, 20–33. <https://doi.org/10.1016/j.ascom.2014.10.004>.

40. Makarov, D.; Savchenko, S.; Mosenkov, A.; Bizyaev, D.; Reshetnikov, V.; Antipova, A.; Tikhonenko, I.; Usachev, P.; Borisov, S.; Makarova, L.; et al. The edge-on Galaxies in the Pan-STARRS survey (EGIPS). *Mon. Not. R. Astron. Soc.* **2022**, *511*, 3063–3075. <https://doi.org/10.1093/mnras/stac227>.

41. Dey, A.; Schlegel, D.J.; Lang, D.; Blum, R.; Burleigh, K.; Fan, X.; Findlay, J.R.; Finkbeiner, D.; Herrera, D.; Juneau, S.; et al. Overview of the DESI Legacy Imaging Surveys. *Astron. J.* **2019**, *157*, 168. <https://doi.org/10.3847/1538-3881/ab089d>.

42. Makarov, D.; Prugniel, P.; Terekhova, N.; Courtois, H.; Vauglin, I. HyperLEDA. III. The catalogue of extragalactic distances. *Astron. Astrophys.* **2014**, *570*, A13. <https://doi.org/10.1051/0004-6361/201423496>.

43. Schlafly, E.F.; Finkbeiner, D.P. Measuring Reddening with Sloan Digital Sky Survey Stellar Spectra and Recalibrating SFD. *Astrophys. J.* **2011**, *737*, 103. <https://doi.org/10.1088/0004-637X/737/2/103>.

44. Pillepich, A.; Sotillo-Ramos, D.; Ramesh, R.; Nelson, D.; Engler, C.; Rodriguez-Gomez, V.; Fournier, M.; Donnari, M.; Springel, V.; Hernquist, L. Milky Way and Andromeda analogues from the TNG50 simulation. *Mon. Not. R. Astron. Soc.* **2024**, *535*, 1721–1762. <https://doi.org/10.1093/mnras/stae2165>.

45. Pillepich, A.; Nelson, D.; Springel, V.; Pakmor, R.; Torrey, P.; Weinberger, R.; Vogelsberger, M.; Marinacci, F.; Genel, S.; van der Wel, A.; et al. First results from the TNG50 simulation: The evolution of stellar and gaseous discs across cosmic time. *Mon. Not. R. Astron. Soc.* **2019**, *490*, 3196–3233. <https://doi.org/10.1093/mnras/stz2338>.

46. Springel, V. E pur si muove: Galilean-invariant cosmological hydrodynamical simulations on a moving mesh. *Mon. Not. R. Astron. Soc.* **2010**, *401*, 791–851. <https://doi.org/10.1111/j.1365-2966.2009.15715.x>.

47. Anderson, S.R.; Gough-Kelly, S.; Debattista, V.P.; Du, M.; Erwin, P.; Cuomo, V.; Caruana, J.; Hernquist, L.; Vogelsberger, M. The interplay between accretion, downsizing, and the formation of box/peanut bulges in TNG50. *Mon. Not. R. Astron. Soc.* **2024**, *527*, 2919–2939. <https://doi.org/10.1093/mnras/stad3271>.

48. Chabrier, G. Galactic Stellar and Substellar Initial Mass Function. *Publ. Astron. Soc. Pac.* **2003**, *115*, 763–795. <https://doi.org/10.1086/376392>.

49. Bruzual, G.; Charlot, S. Stellar population synthesis at the resolution of 2003. *Mon. Not. R. Astron. Soc.* **2003**, *344*, 1000–1028. <https://doi.org/10.1046/j.1365-8711.2003.06897.x>.

50. Torrey, P.; Snyder, G.F.; Vogelsberger, M.; Hayward, C.C.; Genel, S.; Sijacki, D.; Springel, V.; Hernquist, L.; Nelson, D.; Kriek, M.; et al. Synthetic galaxy images and spectra from the Illustris simulation. *Mon. Not. R. Astron. Soc.* **2015**, *447*, 2753–2771. <https://doi.org/10.1093/mnras/stu2592>.

51. Bertin, E.; Arnouts, S. SExtractor: Software for source extraction. *Astron. Astrophys. Suppl. Ser.* **1996**, *117*, 393–404. <https://doi.org/10.1051/aas:1996164>.

52. Bertin, E. Automated Morphometry with SExtractor and PSFEx. In Proceedings of the Astronomical Data Analysis Software and Systems XX, Boston, MA, USA, 7–11 November 2010; Evans, I.N., Accomazzi, A., Mink, D.J., Rots, A.H., Eds.; Astronomical Society of the Pacific: San Francisco, CA, USA, 2011; Volume 442, p. 435.

53. Gadotti, D.A.; Baes, M.; Falony, S. Radiative transfer in disc galaxies—IV. The effects of dust attenuation on bulge and disc structural parameters. *Mon. Not. R. Astron. Soc.* **2010**, *403*, 2053–2062. <https://doi.org/10.1111/j.1365-2966.2010.16243.x>.

54. Savchenko, S.S.; Poliakov, D.M.; Mosenkov, A.V.; Smirnov, A.A.; Marchuk, A.A.; Il'in, V.B.; Gontcharov, G.A.; Seguine, J.; Baes, M. The problem of dust attenuation in photometric decomposition of edge-on galaxies and possible solutions. *Mon. Not. R. Astron. Soc.* **2023**, *524*, 4729–4745. <https://doi.org/10.1093/mnras/stad2189>.

55. Ronneberger, O.; Fischer, P.; Brox, T. U-Net: Convolutional Networks for Biomedical Image Segmentation. *arXiv* **2015**, arXiv:1505.04597.

56. Erwin, P. IMFIT: A Fast, Flexible New Program for Astronomical Image Fitting. *Astrophys. J.* **2015**, *799*, 226. <https://doi.org/10.1088/0004-637X/799/2/226>.

57. Moré, J.J. The Levenberg-Marquardt algorithm: Implementation and theory. In *Numerical Analysis, Proceedings of the Biennial Conference, Dundee, UK, 28 June–1 July 1977; Lecture Notes in Mathematics*; Springer: Berlin/Heidelberg, Germany, 1978; Volume 630, pp. 105–116. <https://doi.org/10.1007/BFb0067700>.

58. Nelder, J.A.; Mead, R. A Simplex Method for Function Minimization. *Comput. J.* **1965**, *7*, 308–313. <https://doi.org/10.1093/comjnl/7.4.308>.

59. Sersic, L.J. *Atlas de Galaxias Australes*; Observatorio Astronomico: Cordoba, Spain, 1968.

60. Caon, N.; Capaccioli, M.; D’Onofrio, M. On the shape of the light profiles of early-type galaxies. *Mon. Not. R. Astron. Soc.* **1993**, *265*, 1013–1021. <https://doi.org/10.1093/mnras/265.4.1013>.

61. Méndez-Abreu, J.; Ruiz-Lara, T.; Sánchez-Menguiano, L.; de Lorenzo-Cáceres, A.; Costantin, L.; Catalán-Torrecilla, C.; Florido, E.; Aguerri, J.A.L.; Bland-Hawthorn, J.; Corsini, E.M.; et al. Two-dimensional multi-component photometric decomposition of CALIFA galaxies. *Astron. Astrophys.* **2017**, *598*, A32. <https://doi.org/10.1051/0004-6361/201629525>.

62. Mosenkov, A.V.; Sotnikova, N.Y.; Reshetnikov, V.P.; Bizyaev, D.V.; Kautsch, S.J. Does the stellar disc flattening depend on the galaxy type? *Mon. Not. R. Astron. Soc.* **2015**, *451*, 2376–2389. <https://doi.org/10.1093/mnras/stv1085>.

63. Gargiulo, I.D.; Monachesi, A.; Gómez, F.A.; Nelson, D.; Pillepich, A.; Pakmor, R.; Grand, R.J.J.; Fragkoudi, F.; Hernquist, L.; Lovell, M.; et al. High and low Sérsic index bulges in Milky Way- and M31-like galaxies: Origin and connection to the bar with TNG50. *Mon. Not. R. Astron. Soc.* **2022**, *512*, 2537–2555. <https://doi.org/10.1093/mnras/stac629>.

64. Erwin, P. What determines the sizes of bars in spiral galaxies? *Mon. Not. R. Astron. Soc.* **2019**, *489*, 3553–3564. <https://doi.org/10.1093/mnras/stz2363>.

65. Ebrová, I.; Bílek, M.; Eliášek, J. Photometric stellar masses for galaxies in DESI Legacy Imaging Surveys. *arXiv* **2025**, arXiv:2510.02257. <https://doi.org/10.48550/arXiv.2510.02257>.

66. Smirnov, A.A.; Sotnikova, N.Y. Is the late buckling stage inevitable in the bar life? *Mon. Not. R. Astron. Soc.* **2019**, *485*, 1900–1905. <https://doi.org/10.1093/mnras/stz546>.

67. Frankel, N.; Pillepich, A.; Rix, H.W.; Rodriguez-Gomez, V.; Sanders, J.; Bovy, J.; Kollmeier, J.; Murray, N.; Mackereth, T. Simulated Bars May Be Shorter but Are Not Slower Than Those Observed: TNG50 versus MaNGA. *Astrophys. J.* **2022**, *940*, 61. <https://doi.org/10.3847/1538-4357/ac9972>.

68. Bundy, K.; Bershady, M.A.; Law, D.R.; Yan, R.; Drory, N.; MacDonald, N.; Wake, D.A.; Cherinka, B.; Sánchez-Gallego, J.R.; Weijmans, A.M.; et al. Overview of the SDSS-IV MaNGA Survey: Mapping nearby Galaxies at Apache Point Observatory. *Astrophys. J.* **2015**, *798*, 7. <https://doi.org/10.1088/0004-637X/798/1/7>.

69. Habibi, A.; Roshan, M.; Hosseinirad, M.; Khosroshahi, H.; Aguerri, J.A.L.; Cuomo, V.; Abbassi, S. The redshift evolution of galactic bar pattern speed in TNG50. *Astron. Astrophys.* **2024**, *691*, A122. <https://doi.org/10.1051/0004-6361/202451028>.

Disclaimer/Publisher’s Note: The statements, opinions and data contained in all publications are solely those of the individual author(s) and contributor(s) and not of MDPI and/or the editor(s). MDPI and/or the editor(s) disclaim responsibility for any injury to people or property resulting from any ideas, methods, instructions or products referred to in the content.